



Measurement of the jet mass distribution and top quark mass in hadronic decays of boosted top quarks in proton-proton collisions at $\sqrt{s} = 13$ TeV

The CMS Collaboration

Abstract

A measurement of the jet mass distribution in hadronic decays of Lorentz-boosted top quarks is presented. The measurement is performed in the lepton+jets channel of top quark pair production ($t\bar{t}$) events, where the lepton is an electron or muon. The products of the hadronic top quark decay are reconstructed using a single large-radius jet with transverse momentum greater than 400 GeV. The data were collected with the CMS detector at the LHC in proton-proton collisions and correspond to an integrated luminosity of 138 fb^{-1} . The differential $t\bar{t}$ production cross section as a function of the jet mass is unfolded to the particle level and is used to extract the top quark mass. The jet mass scale is calibrated using the hadronic W boson decay within the large-radius jet. The uncertainties in the modelling of the final state radiation are reduced by studying angular correlations in the jet substructure. These developments lead to a significant increase in precision, and a top quark mass of 172.76 ± 0.81 GeV.

Submitted to the European Physical Journal C

1 Introduction

The top quark is the most massive elementary particle discovered so far [1, 2]. Because of its high mass m_t and its large Yukawa coupling it plays a crucial role in the electroweak sector of the standard model (SM) of particle physics. Precise measurements of m_t allow for stringent tests of the validity of the SM [3–5] and place constraints on the stability of the electroweak vacuum [6–8].

Direct measurements of m_t using the top quark decay products have already achieved a precision of about 0.5 GeV [9–15]. In these measurements, observables with high sensitivity to the value of m_t are constructed. Measured distributions in these observables are compared to detector level simulations to extract the value of m_t that fits the data best. The predictions rely on a precise modelling of the parton shower and hadronisation process, which cannot be calculated from first principles, and are thus subject to corresponding systematic uncertainties. In addition, uncertainties exist in the translation of m_t extracted from event generators to a value of m_t in a well defined renormalisation scheme [16, 17], as used in precise analytic calculations in quantum field theory.

A different approach is the determination of m_t from cross section measurements corrected for detector effects. These can be directly compared to analytic calculations from first principles. The inclusive cross section of top quark pair ($t\bar{t}$) production can be measured precisely and has been used to extract a value of the top quark pole mass by a comparison to fixed-order calculations in perturbative quantum chromodynamics (QCD). Such measurements have been carried out by the D0 [18, 19], ATLAS [20–22], and CMS [23–25] Collaborations. These measurements of the total $t\bar{t}$ cross section are sensitive to various sources of uncertainties, which can not be constrained in situ during the extraction of m_t , resulting in a precision of about 2 GeV. Recently, a multi-differential cross section measurement has been performed by the CMS Collaboration, achieving an uncertainty of 0.8 GeV in the top quark pole mass [26]. The shape of the measured distributions close to the $t\bar{t}$ production threshold is sensitive to the value of m_t , and a more precise result is achieved compared to the inclusive cross section measurements.

An alternative method which combines the advantages of the two approaches is the determination of m_t from a measurement of the jet mass m_{jet} in events with Lorentz-boosted top quarks [27–29]. At high energies, the decay products of top quarks are Lorentz boosted and merge into a single large-radius jet. The peak position of the distribution in m_{jet} is sensitive to m_t and allows for a precise measurement of m_t [30]. The unfolding of the data to the level of stable particles will allow for a comparison to analytic calculations in perturbative QCD, once these become available. This enables a measurement of the top quark pole mass from the shape of a distribution at the particle level, similar to a recent measurement in $t\bar{t}$ +jet production [31]. Presently, analytic calculations for m_{jet} are restricted to top quark transverse momenta $p_T > 750$ GeV [30], a requirement which results in too few events in data for a differential cross section measurement using the current CERN LHC data sets. Previous measurements by the CMS Collaboration using proton-proton (pp) collision data at $\sqrt{s} = 8$ TeV [32] and 13 TeV [33] with a top quark $p_T > 400$ GeV, have reached an uncertainty of 2.5 GeV, where m_t has been determined using event generators. The results are compatible with those obtained from $t\bar{t}$ production at lower energy scales. In this article, we present a measurement of the differential cross section for $t\bar{t}$ production as a function of the large-radius jet mass with significantly improved statistical and systematic uncertainties. The measurement is used to determine m_t using event generators at next-to-leading order (NLO) precision in QCD. The approach is complementary to measurements close to threshold production with fully resolved final state objects. This provides a precise test of the validity of the approximations made in event generators and

the corresponding systematic uncertainties.

In the lepton+jets channel of $t\bar{t}$ production, the final state is obtained from one top quark decaying to give a b quark and leptons, $t \rightarrow bW \rightarrow b\ell\nu_\ell$, and the second decaying hadronically, $t \rightarrow bW \rightarrow bq\bar{q}'$. Here, the term lepton denotes an electron or muon. This final state combines the advantages of a clear signature from the leptonic W boson decay, with a small background from events with jets from light-flavour quarks and gluons. The large $t\bar{t}$ branching fraction for the lepton+jets channel also results in large event samples. In addition, in case of $t\bar{t}$ production with high top quark p_T , the hadronic decay allows the full reconstruction of the top quark decay within a single large-radius jet with $p_T > 400$ GeV, provided that the decay products are produced within the detector acceptance. The lepton serves as a means to select $t\bar{t}$ events, and the mass of the large-radius jet in the opposite hemisphere of the event is the measurable for this analysis. The lepton is not necessarily isolated, because the large Lorentz boost can result in particles from the fragmentation of the b quark to be produced inside of the isolation cone around the lepton. The analysis strategy follows the one from the previous measurement at 13 TeV [33].

In this article, we analyse 13 TeV pp collision data, recorded in the years 2016 to 2018 and corresponding to an integrated luminosity of 138 fb^{-1} . Besides the improved statistical precision, the leading systematic uncertainties are reduced by using a dedicated calibration of the jet mass scale (JMS) and a detailed study of the effects from final state radiation (FSR) in large-radius jets.

In the previous measurements of m_{jet} in boosted $t\bar{t}$ events [32, 33], the uncertainties in the jet energy scale (JES) have been propagated to m_{jet} . For these the JES uncertainties are the leading experimental systematic uncertainties. While the JES, and therefore the jet momentum, can be determined precisely using the p_T balance or the MPF (missing transverse momentum projection fraction) methods [34, 35], these methods do not necessarily provide the most precise calibrations for m_{jet} . In this article, we calibrate the JMS by reconstructing the W boson mass from two subjets within the large-radius jet. A fit to data in the peak region of the jet mass results in a JMS with smaller uncertainties.

The FSR is modelled by the parton showers in the event generators, which are matched to the simulation of the hard process. The value of the strong coupling used in the FSR shower, evaluated at the mass of the Z boson, $\alpha_S^{\text{FSR}}(m_Z^2)$, is an important parameter that affects the amount of FSR. Changes in its value can cause large differences in the substructure of large-radius jets. Observables probing the angular distributions of the energy density within a jet, such as N -subjettiness [36, 37] ratios, are very sensitive to the amount of FSR in the simulation. In this article, we measure distributions in N -subjettiness ratios calculated for large-radius jets, and use these to constrain the value of $\alpha_S^{\text{FSR}}(m_Z^2)$ used in the modelling of FSR. This leads to smaller uncertainties in m_{jet} from the FSR modelling compared to the usual variations of the scale μ in $\alpha_S^{\text{FSR}}(\mu^2)$ [33, 38, 39].

Tabulated results are provided in the HEPData record for this analysis [40].

2 The CMS detector

The central feature of the CMS detector is a superconducting solenoid of 6 m internal diameter, providing a magnetic field of 3.8 T. A silicon pixel and strip tracker, a lead tungstate crystal electromagnetic calorimeter (ECAL), and a brass and scintillator hadron calorimeter (HCAL), each composed of a central barrel and two endcap sections, reside within the solenoid vol-

ume. Forward calorimeters extend the pseudorapidity (η) coverage provided by the barrel and endcap detectors. Muons are detected in gas-ionisation chambers embedded in the steel flux-return yoke outside the solenoid. A more detailed description of the CMS detector, together with a definition of the coordinate system, can be found in Ref. [41]. Between the 2016 and 2017 data taking runs, the CMS pixel detector was upgraded with additional layers in the barrel and endcap regions of the CMS detector. Details about the changes can be found in Ref. [42].

Events of interest are selected using a two-tiered trigger system. The first level, composed of custom hardware processors, uses information from the calorimeters and muon detectors to select events at a rate of around 100 kHz within a fixed latency of about 4 μ s [43]. The second level, known as the high-level trigger, consists of a farm of processors running a version of the full event reconstruction software optimised for fast processing, and reduces the event rate to around 1 kHz before data storage [44].

3 Data and simulated samples

The measurement is performed in the lepton+jets final state of $t\bar{t}$ production. The event selection is based on the presence of a single lepton which uses the data selected by single-lepton triggers [43, 44]. Muon candidates are required to have $p_T > 50$ GeV and $|\eta| < 2.4$, without any requirement on the isolation of the muon. The average efficiency of this trigger is 91, 90, and 91% for 2016, 2017, and 2018, respectively. In the electron channel, we use a combination of triggers. The first trigger requires electron candidates with $|\eta| < 2.5$ that are isolated and have a minimum p_T of 27, 35, or 32 GeV for the years 2016, 2017, and 2018, respectively. A second trigger selects electron candidates with $p_T > 120$ GeV, without an isolation requirement. In addition a single-photon trigger is used for selecting electrons without a track requirement. This trigger selects photon candidates with a minimum p_T of 175 GeV in 2016, and 200 GeV in 2017 and 2018. The photon trigger ensures a stable selection efficiency for electrons at high p_T because selection criteria applied to clusters in the ECAL are less strict than those used by the electron trigger. The combination of the three electron and photon triggers provides high efficiency over the full range in p_T considered in this analysis, which is comparable to that obtained using the muon triggers. For lepton $p_T < 120$ GeV, the top quark decay is less collimated and the b jet does not overlap with the lepton isolation cone. In this case, the event selection efficiency is greater than 90% for triggers with an isolation requirement. For $p_T > 120$ GeV, the nonisolated electron trigger has an average efficiency of 95%, increasing to nearly 100% for $p_T > 200$ GeV, where the high p_T efficiency is calculated for the combination with the photon trigger. In the offline analysis, muons and electrons are selected with $|\eta| < 2.4$ and $p_T > 55$ GeV, ensuring that selected events are in the plateau region of the trigger efficiency. The total data set corresponds to an integrated luminosity of 138 fb^{-1} , with 36.3 fb^{-1} [45], 41.5 fb^{-1} [46], and 59.7 fb^{-1} [47] recorded in the years 2016, 2017, and 2018, respectively.

For each of the three years of data taking, the processes relevant for this analysis are simulated individually using a Monte Carlo (MC) simulation technique and they are normalised to the integrated luminosity of each year. The $t\bar{t}$ process is simulated at NLO using the POWHEG v2 [48–53] generator with a top quark mass of 172.5 GeV. We adjust the total cross section to 831.8 pb, obtained from a prediction at next-to-NLO (NNLO) precision in QCD, including resummation of next-to-next-to-leading logarithmic soft gluon terms, using the computer program TOP++ 2.0 [54]. We simulate additional $t\bar{t}$ samples with $m_t = 169.5, 171.5, 173.5,$ and 175.5 GeV, which are used for studying the dependence of the measured cross section on the value of m_t used in simulation, and for the extraction of m_t . The background contribution from single t production is generated at NLO using POWHEG, and the W+jets background is generated at leading

order (LO) using MADGRAPH5_aMC@NLO v2.2.2 [55, 56]. The cross section for single t production in association with a W boson is adjusted to approximate NNLO calculations taken from Refs. [57, 58]. The single top quark s - and t -channel cross sections are adjusted to predictions at NLO precision obtained with HATHOR v2.1 [59]. Events from Drell–Yan (DY) production with additional jets are simulated at LO using MADGRAPH5_aMC@NLO and normalised to the NLO cross section [60]. The production of two heavy gauge bosons with additional jets, and events in which jets are produced only through QCD interactions are simulated at LO using the PYTHIA event generator in version 8.212 [61] for the simulation of 2016 data and version 8.230 for 2017 and 2018. The diboson and QCD multijet samples are referred to as “other SM” backgrounds in the following. The NNPDF3.0 [62] parton distribution functions (PDFs) are used for 2016 simulations and the NNPDF3.1 [63] PDFs are used for 2017 and 2018 simulations.

In all processes, the hadronisation, parton showers, and multiple parton interactions are simulated with PYTHIA. In samples simulated with MADGRAPH5_aMC@NLO, the matrix element calculation is matched to the parton showers using the FxFx [64] and MLM [65] algorithms for NLO and LO, respectively. In the simulation of 2016 data, PYTHIA 8.212 is used with the underlying event (UE) tune CUETP8M2T4 [66] for the simulation of $t\bar{t}$ and single top quark production in the t channel. In this tune, $\alpha_S^{\text{FSR}}(m_Z^2) = 0.1365$ is used for the simulation of FSR. All other simulated samples in 2016 use the CUETP8M1 [38, 67] tune. For the 2017 and 2018 data, PYTHIA 8.230 is used with the CP5 [66] tune. Here, a value of $\alpha_S^{\text{FSR}}(m_Z^2) = 0.118$ is used. The detector response is simulated with the GEANT4 package [68, 69].

Additional inelastic pp collision events are simulated using PYTHIA and superimposed on simulated events to model the effect of additional pp collisions within the same or adjacent bunch crossings (pileup). We use a total inelastic cross section of 69.2 mb [70] to estimate the expected number of pp interactions per bunch crossing and correct the simulation to match the corresponding distribution to that observed in data.

4 Event reconstruction

The particle-flow (PF) algorithm [71] aims to reconstruct and identify each individual particle in an event, using an optimised combination of information from the various elements of the CMS detector. The candidate vertex with the largest sum of the square of the transverse momenta p_T^2 of the physics objects is taken to be the leading primary pp interaction vertex. The physics objects are the jets, clustered using the anti- k_T jet finding algorithm [72, 73] with a distance parameter of $R = 0.4$ with tracks assigned to candidate vertices as inputs, and the associated missing transverse momentum, taken as the negative vector sum of the p_T of those jets. More details are given in Section 9.4.1 of Ref. [74].

Muons are reconstructed from tracks in the inner tracker and hits in the muon system using the PF algorithm. The muon momentum is obtained from the curvature of the corresponding track [75]. For electron reconstruction, clusters in the ECAL are connected to tracks in the inner tracker. The electron energy is determined by a combination of the electron momentum at the primary interaction vertex as determined by the tracker, the energy of the corresponding cluster in the ECAL, and the sum of all bremsstrahlung photons spatially compatible with originating from the electron track [76]. The energy of photons is directly obtained from the ECAL measurement [76]. Both muons and electrons have to pass tight quality criteria developed by the CMS Collaboration to ensure a proper reconstruction [75, 76]. The energy of charged hadrons is determined from a combination of their momentum measured in the tracker and the matching ECAL and HCAL energy deposits. Finally, the energy of neutral hadrons is obtained from the corresponding corrected ECAL and HCAL energy [71].

Jets are reconstructed from PF candidates using the anti- k_T [72] or the XCone (eXclusive Cone) [77] algorithm as implemented in the FASTJET software package [73]. Two sets of anti- k_T jets are obtained using distance parameters of $R = 0.4$ (AK4 jets) and 0.8 (AK8 jets). In the jet clustering procedure, charged PF candidates are excluded if they are associated with pileup vertices. While AK4 jets are used mostly for the identification of b jets in this analysis, AK8 jets are used to study the influence of FSR on the jet substructure as described in Section 8. For the XCone jets, a specialized two-step clustering procedure [78] is used. Being an exclusive algorithm, XCone always returns a requested number of jets. This feature of the algorithm can be leveraged to efficiently reconstruct the boosted $t\bar{t}$ final state. At first, the XCone algorithm is run finding exactly two large-radius jets with a distance parameter of $R = 1.2$. This step takes all PF candidates, after removing charged particles assigned to a pileup vertex, as an input and aims to reconstruct the two top quark decays of the $t\bar{t}$ process in separate jets. As a second step, all PF candidates clustered into a large-radius XCone jet are input to the XCone algorithm again, which is now required to find three XCone subjets, $N_{\text{sub}} = 3$, with a distance parameter $R_{\text{sub}} = 0.4$. The second step aims to reconstruct the three-prong decay $t \rightarrow bW \rightarrow bq\bar{q}'$ while minimising the effects of uncorrelated soft radiation or additional energy deposits from pileup. The final XCone jets are then defined as the sum of the four-momenta of their respective subjets. In this way, all particles not clustered into the three subjets are removed from the large-radius XCone jets, similar to the trimming algorithm [79]. The jet mass is calculated from the sum of the four-momenta of all particles clustered into the subjets. Since no lepton selection has been applied at this stage, the XCone reconstruction will also reconstruct $t \rightarrow bW \rightarrow b\ell\nu_\ell$ with three subjets. We have verified that the difference from the more natural choice of two XCone subjets for the reconstruction of the leptonic decay does not significantly affect the identification of the leptonic XCone jet and the event reconstruction. The XCone jet with larger angular distance to the identified single lepton is selected as the measurement jet and is labelled “XCone jet” in the following. The XCone jet closer to the lepton is referred to as “second XCone jet”. Here, the angular distance between two objects is defined as $\Delta R = \sqrt{(\Delta\eta)^2 + (\Delta\phi)^2}$, where ϕ is the azimuthal angle in radians. The four-momenta of identified leptons are subtracted from AK4 jets and XCone subjets if they are within $\Delta R < 0.4$ of the respective (sub)jet.

Jet energy corrections (JECs) [35] derived for AK4 jets are applied to AK4 jets, as well as to XCone subjets in this analysis. These JECs include corrections for contributions from pileup, as derived for AK4 jets clustered after removing all charged particles assigned to a pileup vertex. Jet energies in simulated events are smeared to match the jet energy resolution (JER) observed in data. The XCone subjets are corrected with the same procedure as in Ref. [33], where an additional XCone correction is derived because of residual differences to AK4 jets. The correction is obtained from simulated samples of $t\bar{t}$ in the all-jets channel and parametrised as a function of the XCone subjet p_T and $|\eta|$. The XCone jet mass is calibrated as described in Section 7. The JMS correction is applied to the four-momentum of the jet such that it changes only the mass but leaves the three-momentum unaltered.

5 Particle-level phase space

The measurement of m_{jet} is carried out at the particle level in the fiducial region defined below. The particle level is defined by the set of all stable particles, i.e. with a lifetime longer than 10^{-8} s as provided by the event simulation. We develop an unfolding procedure to correct the data for detector and pileup effects. This procedure provides a measurement at the particle level using data recorded at the detector level.

The fiducial region at the particle level is defined such that similar requirements can be used

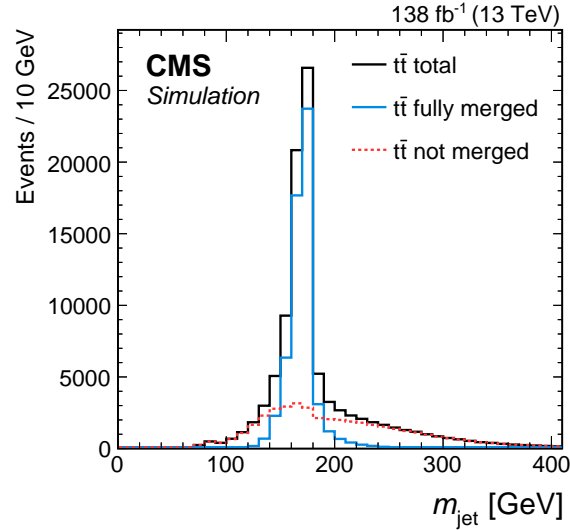


Figure 1: Distribution in m_{jet} at the particle level after the selection of the fiducial region in the lepton+jets channel of $t\bar{t}$, simulated with POWHEG. The contributions from fully merged events (blue solid) and not merged events (red dashed) are displayed, as well as the sum of the two (black solid).

on data at the detector level, which helps to keep the corrections small in the unfolding step. In order to select the lepton+jets channel of the $t\bar{t}$ process, exactly one prompt electron or muon with $p_T > 60$ GeV originating from the decay of a W boson must be present. Decays to τ leptons contribute a small background. They are not selected and are treated as background in this analysis. The two-step XCone clustering procedure is performed similarly to the one at the reconstruction level, as explained in Section 4, with all stable particles except for neutrinos as input. Decays of boosted top quarks must have an XCone jet with $p_T > 400$ GeV. All three XCone subjects have to satisfy $p_T > 30$ GeV and $|\eta| < 2.5$. The requirement on $|\eta|$ ensures that the XCone jet is reconstructed within the geometric acceptance of the detector. The second XCone jet has to have $p_T > 10$ GeV after the lepton four-momentum has been subtracted. This requirement rejects pathological cases, where the second XCone jet does not contain the b subject from the t decay. The XCone-jet mass m_{jet} has to be larger than the invariant mass of the sum of the second XCone jet and the selected lepton. Since the neutrino from the leptonic decay is not reconstructed, this requirement is always fulfilled if all decay products of the hadronic decay are reconstructed within the XCone jet, referred to as “fully merged”. This criterion helps to select fully merged decays without introducing a bias on the measurement XCone jet, which would be the case with additional requirements on its substructure. Figure 1 shows the distribution in m_{jet} at the particle level after the selection of the fiducial region. The distribution has a narrow peak, with the maximum close to m_t . Contributions from the UE and FSR lead to a shift of the peak towards higher values. In the peak region, the contribution of fully merged top quark decays is about 87%. Contributions from $t\bar{t}$ that is not fully merged, where the top quark has only been partially reconstructed within the XCone jet, originate from radiation not associated with the $t\bar{t}$ system and dominate the regions to the left and right of the peak. With respect to the measurement at 8 TeV [32], which used Cambridge–Aachen jets [80, 81] with $R = 1.2$, the width of the distribution in the peak region is reduced by a factor of two with the two-step XCone clustering procedure.

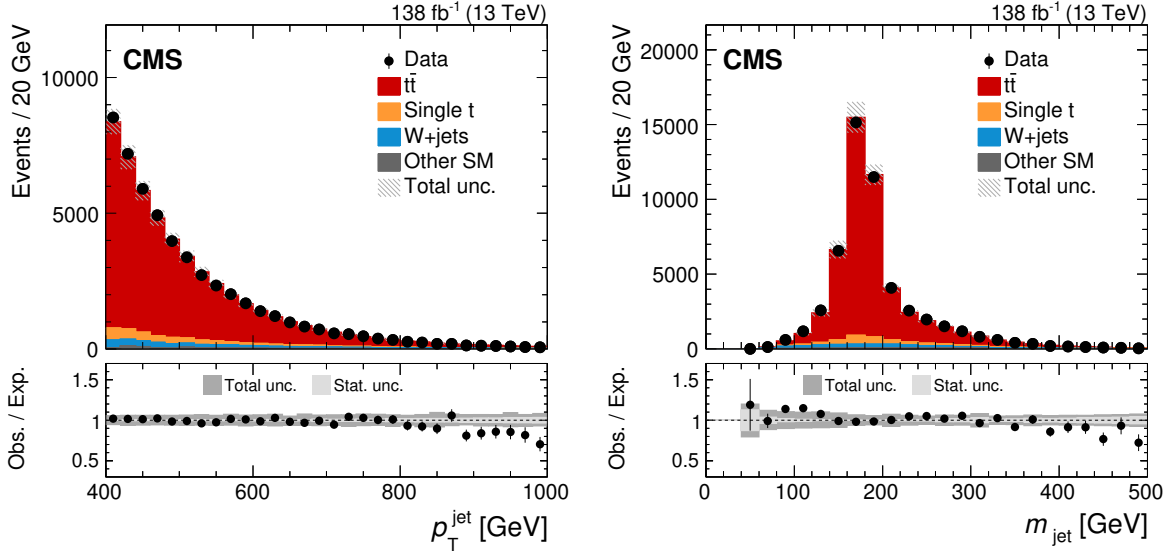


Figure 2: Distributions in the reconstructed X Cone jet p_T (left) and m_{jet} (right), after the full event selection. The vertical bars on the markers show the statistical uncertainty. The hatched regions show the total uncertainty in the simulation, including the statistical and experimental systematic uncertainties. The lower panels show the ratio of the data to the simulation. The uncertainty bands include the experimental systematic uncertainties and statistical uncertainties in the simulation. In the ratios, the statistical (light grey) and total (dark grey) uncertainties are shown separately.

6 Event selection

At the detector level, the event selection aims to include a similar phase space as selected at the particle level. Events must contain a single muon or single electron with $p_T > 60$ GeV and $|\eta| < 2.4$. Leptons with $55 < p_T < 60$ GeV and $|\eta| < 2.4$ are used to construct a sideband region when unfolding the data, as described in Section 9. Electrons with $p_T < 120$ GeV must pass an isolation requirement [76], where the isolation is defined as the p_T sum of charged hadrons and neutral particles in a cone with radius $R = 0.3$ around the electron. The isolation variable is corrected to mitigate the contribution from pileup. Electron candidates with $p_T > 120$ GeV and muons are rejected if there is an AK4 jet within $\Delta R < 0.4$ and $p_T^{\text{rel}} < 40$ GeV, where p_T^{rel} is the component of the lepton momentum orthogonal to the AK4-jet axis. The last criterion has high efficiency of selecting highly boosted $t \rightarrow bW(\rightarrow \ell\nu_\ell)$ decays, where the lepton would not have passed an isolation requirement because of the angular proximity of the b jet, while rejecting QCD multijet events [82, 83].

In order to suppress non- $t\bar{t}$ backgrounds, at least one AK4 jet is required to be b tagged using the DEEPJET algorithm [84, 85]. The candidate b jets are required to have $p_T > 30$ GeV and $|\eta| < 2.4$, and must pass a selection on the DEEPJET discriminator value corresponding to a misidentification rate of 0.1% for light-flavour quark and gluon jets, and an efficiency of 68%.

In addition, the magnitude of the negative vector sum of the transverse momenta of the PF candidates in an event [86], p_T^{miss} , has to be larger than 50 GeV. The energy scale corrections applied to AK4 jets are propagated to p_T^{miss} . This requirement suppresses the contribution of multijet backgrounds from the production of light-flavour quarks and gluons.

The X Cone jet is required to have $p_T > 400$ GeV and all three subjets must have $p_T > 30$ GeV and $|\eta| < 2.5$. The second X Cone jet has to have $p_T > 10$ GeV and the invariant mass of the system containing the second X Cone jet and the lepton must not surpass m_{jet} .

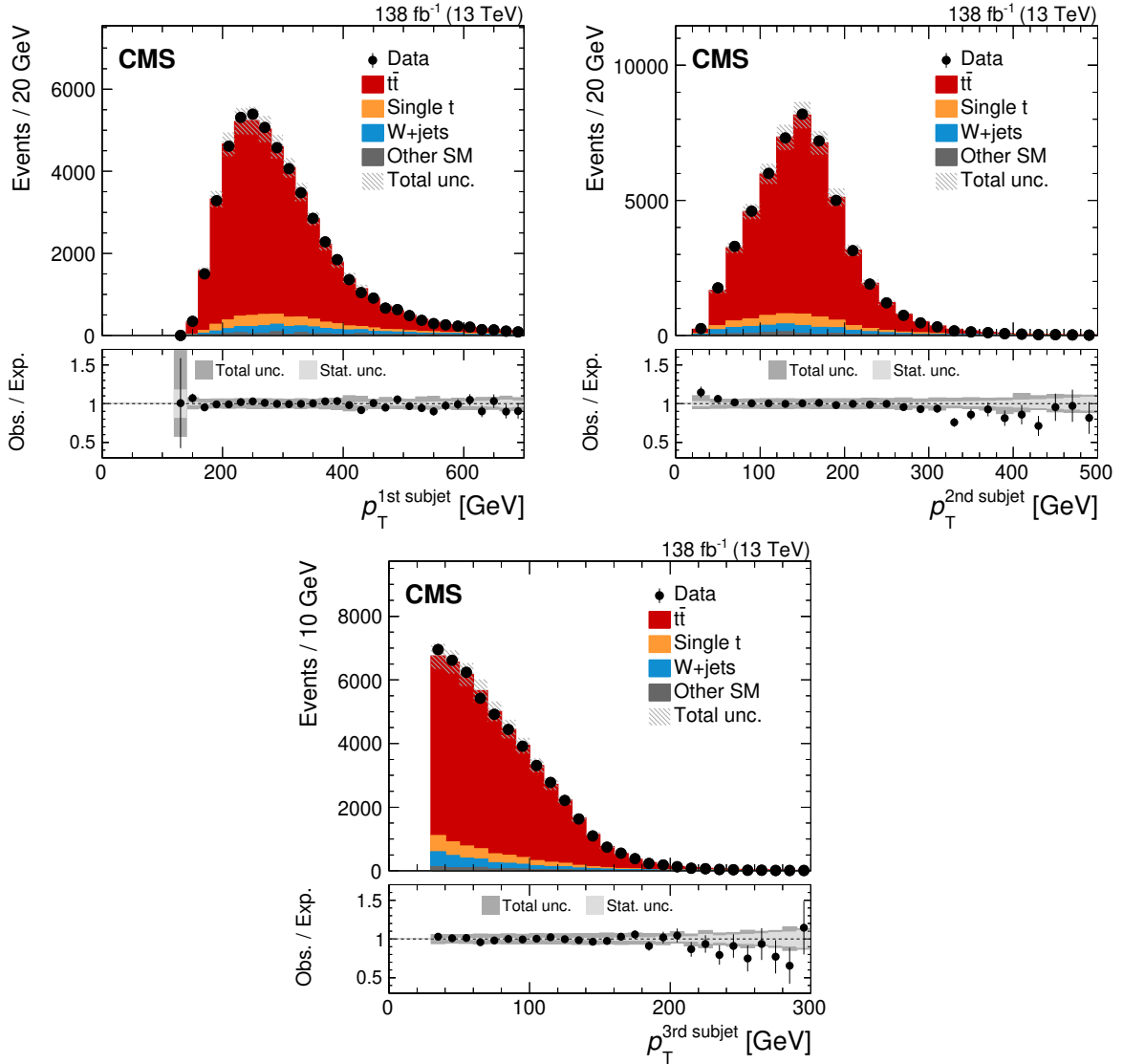


Figure 3: Distributions in reconstructed p_T of the p_T -leading X Cone subjet (upper left), second X Cone subjet (upper right) and third X Cone subjet (lower). The vertical bars on the markers show the statistical uncertainty. The hatched regions show the total uncertainty in the simulation, including the statistical and experimental systematic uncertainties. The lower panels show the ratio of the data to the simulation. The uncertainty bands include the experimental systematic uncertainties and statistical uncertainties in the simulation. In the ratios, the statistical (light grey) and total (dark grey) uncertainties are shown separately.

Figure 2 shows the X Cone jet p_T (left) and m_{jet} (right) spectra at the detector level. Here, data from all three years and both lepton flavours are combined. For the sake of comparing the shapes of these distributions, the $t\bar{t}$ simulation has been scaled down such that the number of simulated events matches the number of events observed in the data. The distribution in p_T shows the characteristic falling behaviour above the 400 GeV threshold, while the distribution in m_{jet} shows a narrow peak close to m_t . We find reasonable agreement between data and simulation in the p_T and m_{jet} distributions when we use the JECs, and the X Cone and JMS corrections described in Section 7. For p_T above 900 GeV, we observe that the simulation predicts more events than observed in data, a feature which has been reported previously in differential $t\bar{t}$ cross section measurements when comparing to NLO calculations [87–89]. Figure 3

shows the distributions in p_T of the X Cone subjets. Because of the X Cone-jet selection with $p_T > 400$ GeV, the first subjet has a most probable p_T of about 250 GeV, and the second subjet has a value of about 150 GeV. The remaining subjet features a falling distribution, starting from the minimum value of 30 GeV.

7 Calibration of the jet mass scale

The experimental precision in the measurement of m_{jet} in boosted top quark decays is limited by the calibration of the jet four-momentum. In our previous analysis [33], the uncertainty in the JES was propagated to m_{jet} and resulted in the dominant experimental systematic uncertainty. In this article, we measure the JMS using the invariant mass of the two X Cone subjets originating from the hadronic W boson decay. With this additional measurement, the uncertainty in the JES is split into a part that only affects the jet three-momentum and a part that only affects m_{jet} . The JMS calibration is crucial for the improvement in the overall precision of this measurement.

For the JMS calibration, the same selection as for the measurement is applied. The W boson decay is reconstructed using two of the three X Cone subjets from the X Cone jet initiated by the hadronic top quark decay. We identify the X Cone subjet originating from the fragmentation of the b quark using the DEEPJET algorithm on AK4 jets. First, the AK4 jet with the largest value of the DEEPJET b discriminant among those with angular distance $\Delta R < 1.2$ to the X Cone jet is selected. In a second step, the X Cone subjet with the smallest ΔR to the selected b-tagged AK4 jet is assigned to originate from the b quark. This X Cone subjet is rejected, and the measurement of the JMS is performed using the invariant mass of the other two X Cone subjets. Data from the two lepton flavours and three different years are combined for the JMS calibration.

The JMS in simulation is adjusted by introducing two factors, f^{JEC} and f^{XCone} , that vary the jet energy scale in the AK4 JECs and the additional X Cone-jet corrections, respectively. The factors are constructed such that values of 0, +1 and -1 represent the nominal correction, and the up and down shifts by one standard deviation, respectively.

The measurement is performed in four regions that are defined in the two-dimensional plane of the p_T of the reconstructed W boson, p_T^{W} , and the ratio $r_{p_T} = p_T^{s_1} / p_T^{\text{W}}$, defined as the ratio of the p_T carried by the highest p_T X Cone subjet s_1 to p_T^{W} . These regions are constructed to reduce correlations between f^{JEC} and f^{XCone} , because these factors can cancel each other in an inclusive measurement of the JMS. The effects of f^{JEC} and f^{XCone} are different in the four regions defined by p_T^{W} and r_{p_T} , such that these two factors can be determined simultaneously. Figure 4 shows the distribution in the reconstructed W boson mass m_W in the vicinity of its peak in the four regions, defined by p_T^{W} larger or smaller than 300 GeV and r_{p_T} larger or smaller than 0.7. We consider only bins with more than 100 events in data for the JMS calibration, in order to remove the tails in the m_W distribution, which originate from a wrong assignment of subjets to the reconstructed W boson. This amounts to a total of 157 bins with a bin width of 1 GeV. The distributions of background-subtracted data and $t\bar{t}$ signal have been normalised to unit area and are given in arbitrary units (a.u.), such that only shapes are considered and the total yield does not affect the measurement. The $t\bar{t}$ simulation is shown for the different variations in the jet corrections, parametrised by f^{JEC} and f^{XCone} . The peak in m_W is shifted to higher values for larger factors of f^{JEC} , while smaller factors shift the distribution to lower values. The same is observed for the parameter f^{XCone} .

In each bin i of the m_W distribution, a linear prediction g_i as a function of f^{JEC} and f^{XCone} is

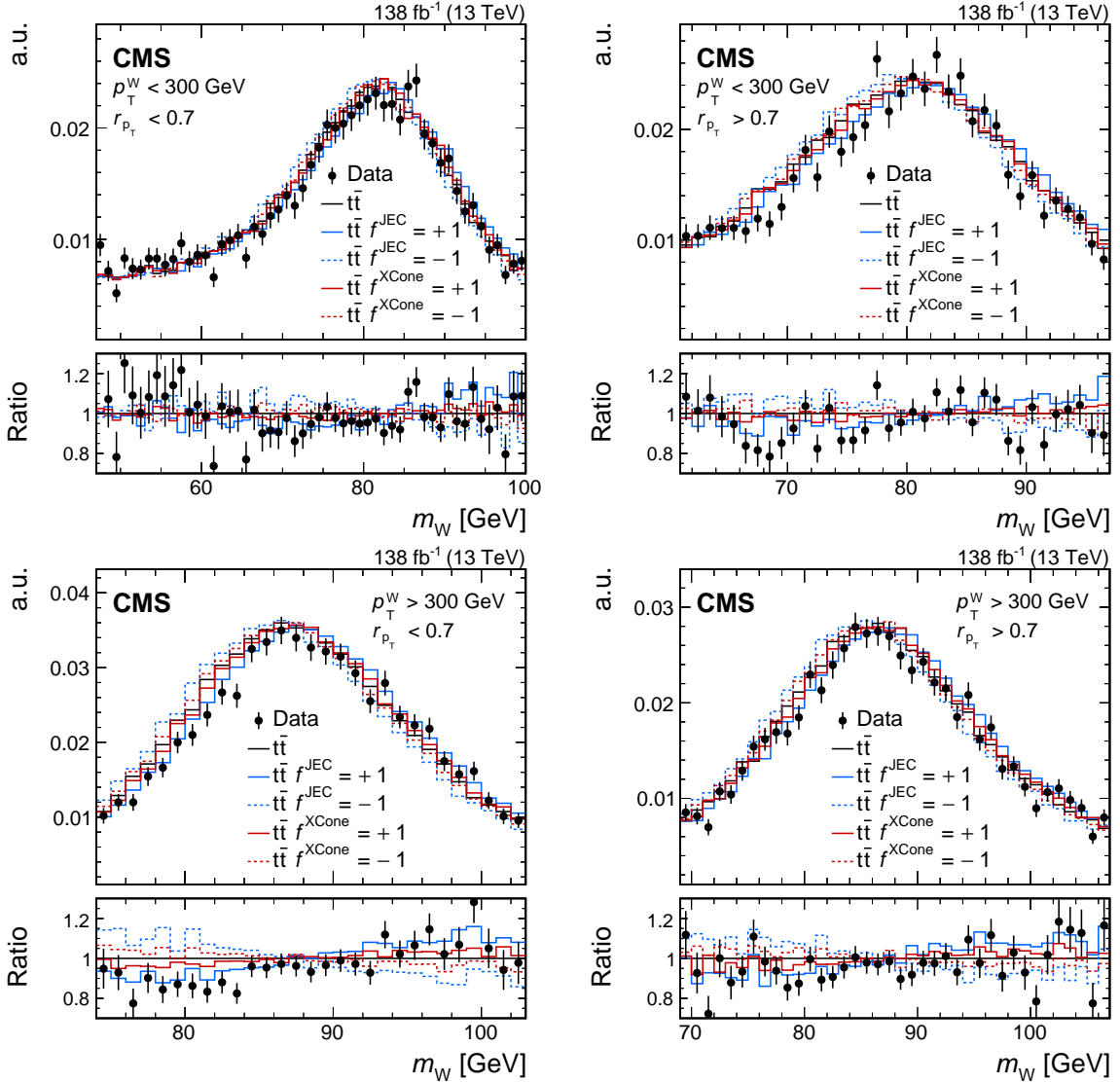


Figure 4: Peak region of the reconstructed W boson mass in the four regions $p_T^W < 300$ GeV and $r_{p_T} < 0.7$ (upper left), $p_T^W < 300$ GeV and $r_{p_T} > 0.7$ (upper right), $p_T^W > 300$ GeV and $r_{p_T} < 0.7$ (lower left), and $p_T^W > 300$ GeV and $r_{p_T} > 0.7$ (lower right). The background-subtracted data and the $t\bar{t}$ simulation are normalised to unit area. For illustration, the $t\bar{t}$ simulation is also shown with the JEC and X Cone correction factors varied by one standard deviation. The lower panels show the ratios to the nominal $t\bar{t}$ simulation.

defined,

$$g_i(f^{\text{JEC}}, f^{\text{XCone}}) = a_i + b_i f^{\text{JEC}} + c_i f^{\text{XCone}}, \quad (1)$$

with the free parameters a_i , b_i , and c_i . The free parameters are obtained from a fit to simulation in the $f^{\text{JEC}}-f^{\text{XCone}}$ plane. We have verified that a linear fit in both factors describes the dependence of m_W on f^{JEC} and f^{XCone} sufficiently well, with a fit quality matching the expectation of statistical fluctuations only.

The factors f^{JEC} and f^{XCone} are obtained from a fit to the data, where a two-dimensional χ^2 function is constructed,

$$\chi^2 = d^T V^{-1} d. \quad (2)$$

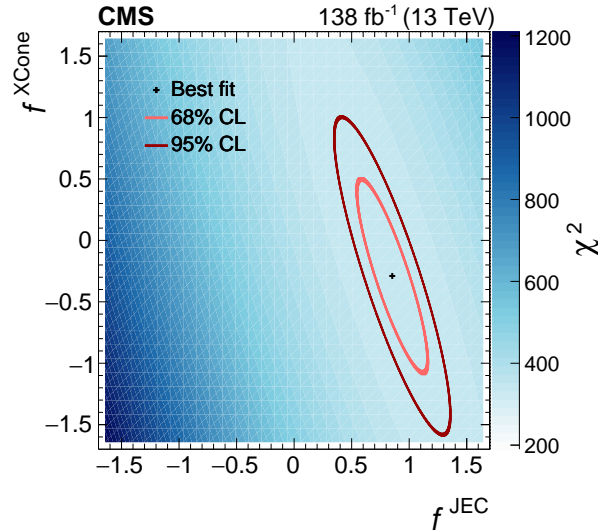


Figure 5: The two-dimensional χ^2 as a function of f^{JEC} and f^{XCone} , obtained from a comparison of background-subtracted data with the predictions from $t\bar{t}$ production in the reconstructed m_W distributions. The minimum is indicated by a black cross, and the borders of the 68 and 95% CL intervals are shown by the light and dark red ellipses, respectively.

The vector d is built from the differences between the predictions $g_i(f^{\text{JEC}}, f^{\text{XCone}})$ and the background-subtracted data in each bin i of all four regions in p_T^W and r_{p_T} . The covariance matrix V includes the statistical uncertainty in data, also considering correlations from the normalisation to unit area, and the uncertainties in the functions g_i from the fit to simulation. The latter are estimated from the statistical uncertainty of the simulated $t\bar{t}$ sample. We also include modelling uncertainties from the $t\bar{t}$ simulation and uncertainties from the background subtraction, but these are small compared to the statistical uncertainties.

Figure 5 shows the evaluated two-dimensional χ^2 , as a function of f^{JEC} and f^{XCone} . The minimum of the χ^2 function lies within the one-standard deviation intervals of the correction factors. We find the best-fit values $f^{\text{JEC}} = 0.85 \pm 0.2$ and $f^{\text{XCone}} = -0.29 \pm 0.52$ with a linear correlation coefficient of -0.87 . The JMS uncertainty obtained from the two-dimensional 68% confidence level (CL) interval is reduced compared to the variations of f^{JEC} and f^{XCone} in the intervals between -1 and $+1$. In order to construct variations of one standard deviation in one dimension for the evaluation of systematic uncertainties, the endpoints of the semi-minor axis are chosen. These result in the largest shift in the m_{jet} distribution, because along the semi-minor axis both factors f^{JEC} and f^{XCone} shift the value of m_{jet} in the same direction. Changes of f^{JEC} and f^{XCone} along the semi-major axis result in shifts in opposite directions, which cancel to a large part. The extracted value pairs in $(f^{\text{JEC}}, f^{\text{XCone}})$, with the nominal value pair of $(0.85, -0.29)$, are $(0.98, -0.24)$ and $(0.72, -0.34)$, which are used in the determination of systematic uncertainties. These pairs of values are referred to as JMS correction in the following, with the corresponding uncertainties. We have verified that variations of m_t in the $t\bar{t}$ simulation do not alter this result. Additionally, we have tested that the results obtained from the electron and muon channels are compatible. The final results of the m_{jet} measurement agree within the uncertainties if the JMS calibration is carried out in the electron channel and applied to the muon channel, and vice versa.

Figure 6 shows the reconstructed m_W distribution after applying the JMS correction. The data are well described by the simulation over the full distribution in m_{jet} . The mean values of m_{jet}

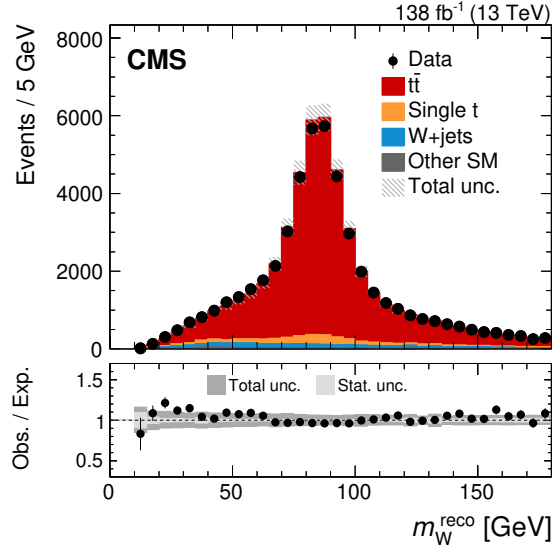


Figure 6: Jet mass distribution of hadronic decays of the W boson, reconstructed from two X Cone subjets. The vertical bars on the markers show the statistical uncertainty. The hatched regions show the total uncertainty in the simulation, including the statistical and experimental systematic uncertainties. The lower panel shows the ratio of the data to the simulation. The uncertainty bands include the experimental systematic uncertainties and statistical uncertainties in the simulation. The statistical (light grey) and total (dark grey) uncertainties are shown separately in the ratio.

for the reconstructed top quark and W boson masses are shown as a function of the number of primary vertices in Fig. 7 (left). The values for the top quark mass are obtained using all three X Cone subjets, while the W boson mass is calculated from the two subjets not matched to the b-tagged AK4 jet. The mean values of m_{jet} are larger than the parameters m_t and m_W used in the simulation by about 4 and 2 GeV, respectively, because of contributions from the UE and pileup interactions. The slope of the mean value of m_{jet} as a function of the number of pileup interactions is small, indicating that the X Cone reconstruction and calibration remove most of the contributions from pileup. The mean values and the slopes are well described by the simulation. The achieved resolution in m_{jet} is displayed in Fig. 7 (right). We calculate the resolution as the width parameter of a Gaussian function, fitted to distributions in $m_{\text{jet}}^{\text{rec}}/m_{\text{jet}}^{\text{gen}}$, where $m_{\text{jet}}^{\text{rec}}$ denotes the reconstructed value of m_{jet} at the detector level and $m_{\text{jet}}^{\text{gen}}$ is the jet mass at the particle level. The achieved resolution is below 8% over the full range in p_T . For an inclusive selection in the number of primary vertices, the mass resolution improves from 7.7% at $p_T = 400$ GeV to 7% for $p_T > 800$ GeV. For a selection with less than 10 primary vertices, the resolution is about one percentage point better than for a selection with more than 20 primary vertices.

8 Studies of the final state radiation

The uncertainty in the modelling of FSR was the dominant model uncertainty in the previous m_{jet} measurement at 13 TeV [33]. There, the energy scale parameter μ , which enters into the definition of the strong coupling $\alpha_S^{\text{FSR}}(\mu^2)$, was changed by factors of 0.5 and 2 in the FSR simulation to estimate this uncertainty. This is equivalent to changing the value of the effective strong coupling at the mass of the Z boson from $\alpha_S^{\text{FSR}}(m_Z^2) = 0.1365$, as used in the parton shower and UE event tune CUETP8M2T4 for the simulation of 2016 data, to values of 0.1556

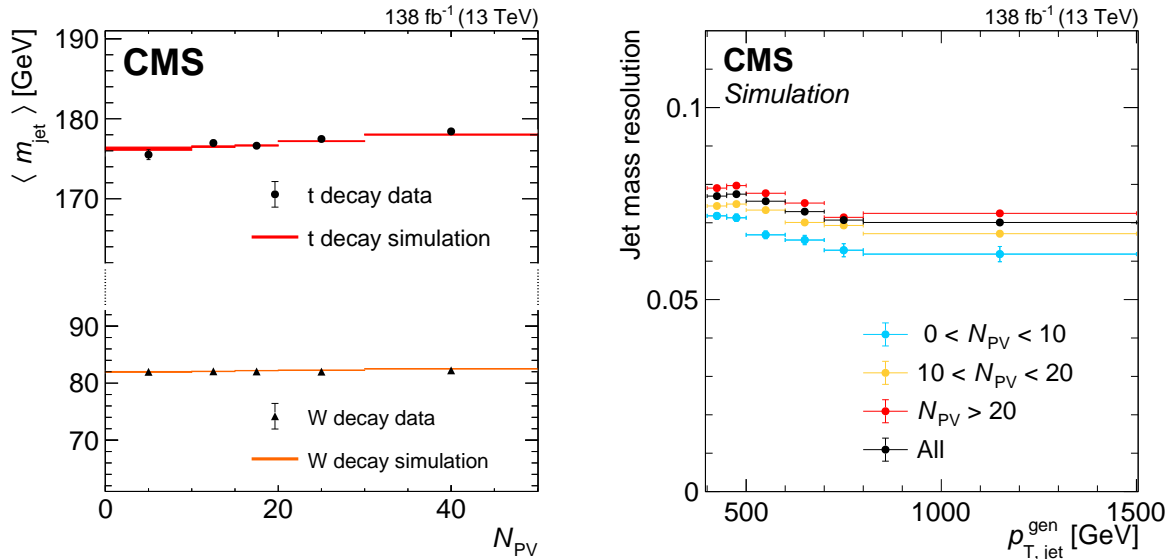


Figure 7: Mean values of the m_{jet} distribution for t and W boson decays, as a function of the number of primary vertices N_{PV} (left). Data (markers) are compared with $t\bar{t}$ simulation (filled areas). The vertical bars and size of the filled areas show the statistical uncertainties in the calculation of the mean values. Jet mass resolution in simulation as a function of particle-level X Cone-jet p_{T} , given for different intervals in the number of primary vertices (right). The vertical bars indicate the statistical uncertainties and the horizontal bars indicate the bin width.

and 0.1217, respectively. While the data are well described using the central value, we find that the large uncertainty variations do not describe the data in the fiducial region of this measurement. For the simulation of 2017 and 2018 data, the CP5 tune is used with $\alpha_{\text{S}}^{\text{FSR}}(m_{\text{Z}}^2) = 0.118$, which is not the optimal choice for the modelling of jet substructure observables in $t\bar{t}$ production, where a larger value is preferred [66]. To remedy this situation, we perform a study of the FSR modelling and find the value of $\alpha_{\text{S}}^{\text{FSR}}(m_{\text{Z}}^2)$ that fits the data best. The study is performed separately for the two samples with different tunes, namely for the year 2016, and for the combination of the years 2017 and 2018. The uncertainties in $\alpha_{\text{S}}^{\text{FSR}}(m_{\text{Z}}^2)$ from this study are propagated to the FSR uncertainty in the m_{jet} measurement.

As a starting point, we modify the energy scale in the FSR simulation by a factor f_{FSR} . With this definition, the FSR modelling uncertainty as used in the previous measurement is obtained by setting $f_{\text{FSR}} = 0.5$ and 2. The prediction becomes a function of f_{FSR} , which we use to determine the best fit value of f_{FSR} through a comparison of distributions between data and simulation in the N -subjettiness ratio $\tau_{32} = \tau_3/\tau_2$ [36, 37]. The distributions in τ_{32} are sensitive to the angular distribution of the energy density inside jets and are thus well suited for determining f_{FSR} .

We use the same event selection as used for the m_{jet} measurement, described in Section 6. Instead of X Cone jets, we use AK8 jets to study the τ_{32} distributions. These have a higher sensitivity to effects from FSR, because AK8 jets are obtained without jet grooming, unlike the X Cone jets clustered with the two-step procedure. The AK8 jet that is within $\Delta R < 0.8$ of the X Cone jet is selected, provided it has $m_{\text{jet}} > 140$ GeV. This requirement on m_{jet} ensures that only jets including all particles from the hadronic t decay are accepted.

Figure 8 shows the normalised distributions in τ_{32} for 2016 (left), and the combination of 2017 and 2018 (right). In both cases, larger values of f_{FSR} shift the distributions to lower values in τ_{32} , and smaller values of f_{FSR} lead to a larger average value of τ_{32} . This is compatible with the expectation of less radiation for larger values of f_{FSR} , corresponding to smaller values of $\alpha_{\text{S}}^{\text{FSR}}$.

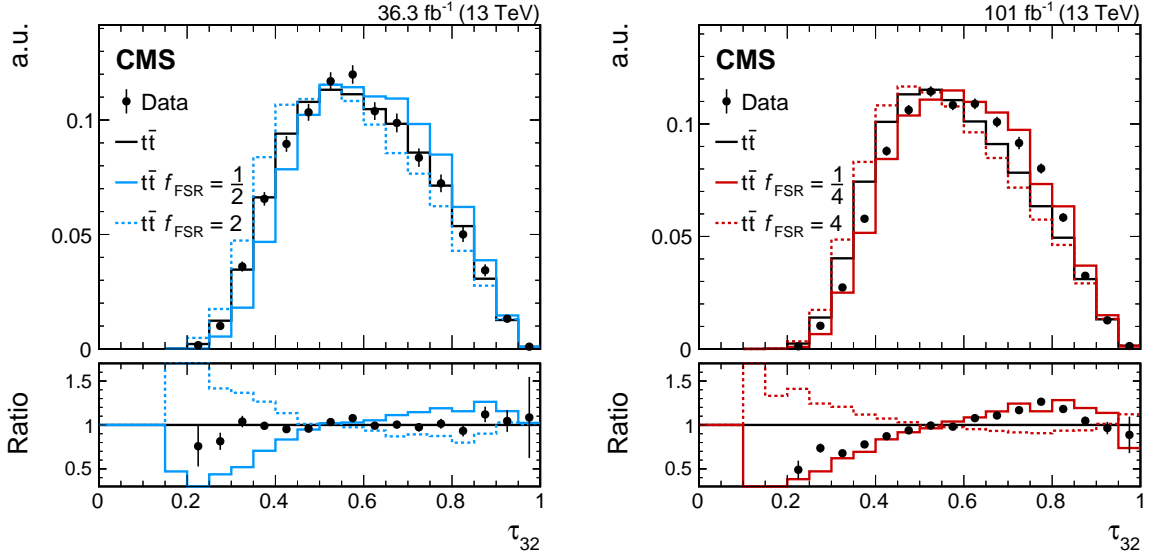


Figure 8: The normalised distributions in τ_{32} for AK8 jets with $m_{\text{jet}} > 140 \text{ GeV}$ from the hadronic decay of boosted top quarks. Shown are distributions for 2016 (left) and the combination of 2017 and 2018 (right). The background-subtracted data are compared to $t\bar{t}$ simulations with the UE tunes CUETP8M2T4 for 2016 and CP5 for the combination of 2017 and 2018, and different values of f_{FSR} are shown as well. The lower panels show the ratio to the $t\bar{t}$ simulation with $f_{\text{FSR}} = 1$.

Without additional radiation, τ_{32} becomes small and compatible with a three-prong decay. If radiation is added to the jet, the value of τ_3 increases, and shifts the average τ_{32} to larger values.

The sensitivity of the τ_{32} distribution to FSR can be used to determine the value of f_{FSR} that is most compatible with the data. We construct predictions $g_i(f_{\text{FSR}})$ in each bin i of the normalised τ_{32} distributions,

$$g_i(f_{\text{FSR}}) = a_i + b_i \log f_{\text{FSR}}^{-2} + c_i f_{\text{FSR}}^{-2}, \quad (3)$$

with the free parameters a_i , b_i , and c_i . The functional form of g_i is inspired by the logarithmic dependence of α_S^{FSR} on the square of the modified energy scale $(f_{\text{FSR}}\mu)^2$. The values of the free parameters are determined in a fit to simulation, sampled at the points $f_{\text{FSR}} \in \{\frac{1}{2}, 1, 2\}$ in 2016 and $f_{\text{FSR}} \in \{\frac{1}{4}, \frac{1}{2}, \frac{1}{\sqrt{2}}, 1, \sqrt{2}, 2, 4\}$ in 2017 and 2018.

The compatibility with the data is tested with a χ^2 function, equivalent to the definition in Eq. (2). The vector of differences is built from the normalised background-subtracted data, and the predictions $g_i(f_{\text{FSR}})$. The uncertainties taken into account by the covariance matrix include statistical uncertainties from data with correlations from the normalisation, and systematic uncertainties in the JECs and in the predictions $g_i(f_{\text{FSR}})$. The latter are conservatively estimated by using the largest statistical uncertainty in a given bin i from any of the points obtained from the simulated samples with different values of f_{FSR} . This choice was made because the point with $f_{\text{FSR}} = 4$ has the smallest statistical precision due to the presence of a large spread of weights in the simulation. The statistical uncertainty in data is the dominant uncertainty in this measurement.

The best fit value of f_{FSR} is obtained by minimising the χ^2 function. Uncertainties corresponding to one standard deviation are evaluated at $\chi_{\text{min}}^2 + 1$. We obtain the best fit values $f_{\text{FSR}} = 0.97 \pm 0.07$ for 2016, and $f_{\text{FSR}} = 0.33 \pm 0.02$ for the combined data of 2017 and 2018. The data are well described by the nominal simulation in 2016, but prefer a larger value of

α_S^{FSR} in the 2017 and 2018 simulations. The best fit values of f_{FSR} can be translated to values of $\alpha_S^{\text{FSR}}(m_Z^2)$. This gives $\alpha_S^{\text{FSR}}(m_Z^2) = 0.1373_{-0.0018}^{+0.0017}$ for 2016 and $\alpha_S^{\text{FSR}}(m_Z^2) = 0.1416_{-0.0018}^{+0.0019}$ for the combination of 2017 and 2018, evaluated using five active flavours in the four-loop evolution of α_S [90]. The uncertainties take into account statistical and leading systematic sources, where the latter are dominated by changes of the modelling in simulation, as described in Section 10. We note that these values do not represent a generally valid measurement of α_S^{FSR} , which would need a different treatment of theory uncertainties from missing higher orders, but the results can be used to calibrate the two different tunes used for the $t\bar{t}$ simulation with POWHEG+PYTHIA. In fact, the two values are compatible and much closer to each other than the values used in the CUETP8M2T4 and CP5 tunes. The uncertainty for 2016 is comparable to the one from the combination of 2017 and 2018, which constitutes a larger data set, because the latter is dominated by statistical uncertainties in the simulation originating from a large spread of weights used to obtain the samples with changes in f_{FSR} . We have verified that extracting f_{FSR} from different intervals in m_{jet} and p_T leads to compatible results, validating the calibration of the FSR modelling in the full fiducial region of this measurement.

9 Unfolding

The data are unfolded to the particle level using regularised unfolding as implemented in the TUNFOLD [91] framework. We have chosen the curvature regularisation condition, such that the second derivative of the unfolded result is regularised. This option introduces the smallest model dependencies in this measurement. The optimal regularisation strength is found by minimising the average global correlation coefficient in the output bins [92]. In addition to the measurement phase space defined in Section 6, five sideband regions are constructed by loosening the most important selection steps. These regions include events where the XCone jet has $350 < p_T < 400$ GeV, the lepton has $55 < p_T < 60$ GeV, at least one of the XCone subjects has $10 < p_T < 30$ GeV, m_{jet} is less than the invariant mass of the sum of the second XCone jet and lepton, and the AK4 jet passes a b-tagging requirement with a misidentification rate of 1%, but not the tight requirement with 0.1%. Additionally, the measurement region and the region with XCone jet $350 < p_T < 400$ GeV are divided into bins of p_T . The two bins in the peak region of m_{jet} with bin boundaries at 152, 172 and 192 GeV are split into four bins in the unfolding, but merged afterwards to avoid large bin-to-bin correlations. The splitting into regions of p_T^{jet} and the subdivision of m_{jet} bins result in a reduced dependence on the modelling parameters in the $t\bar{t}$ simulation and help to reduce the corresponding uncertainties. In addition, this procedure ensures that the most important migrations between the detector and particle levels into and out of the fiducial region of the measurement are included in the unfolding and not purely estimated from simulation. In total, the response matrix includes 200 bins at the detector level and 72 bins at the particle level.

We unfold the three years individually in order to check for a potential bias originating from the different tunes in the $t\bar{t}$ simulation that is used to construct the response matrix. With the dedicated calibration of the FSR parameter in the simulation, all three years are compatible and agree within one standard deviation. We have also ensured that unfolding the electron and muon channels separately leads to a consistent result. For the final measurement, all data and simulated samples are combined before the unfolding.

10 Uncertainties

Several sources of statistical and systematic uncertainties are considered in the measurement of m_{jet} . These are split into four categories: statistical, experimental, model, and theory uncertainties.

Statistical uncertainties are defined as the uncertainties due to the finite statistical precision of the data. With respect to the previous measurement [33], the statistical precision is increased by including data from 2017 and 2018, which increases the size of the data set by a factor of almost four. The statistical uncertainties are propagated through the unfolding process using Gaussian error propagation.

Experimental uncertainties encompass uncertainties in correction factors that are connected to the calibration of physics objects. These include the JECs [35], JER, additional X Cone-jet corrections, JMS, as well as the factors correcting for the efficiencies in the trigger selection [44], lepton identification [75, 76], and b tagging [93]. The JMS correction has been obtained by calibrating m_{jet} in the reconstructed m_W , which is dominated by X Cone subjects originating from light-flavour quarks. To account for a possible difference in the detector response to X Cone subjects originating from the fragmentation of b quarks, an additional flavour uncertainty [35] is applied to X Cone subjects matched to AK4 b-tagged jets (JMS b flavour uncertainty), where the matching is identical to the procedure outlined in Section 7. The uncertainties in the reweighting of the pileup profile are considered. The experimental uncertainties are calculated by changing the corrections up and down by one standard deviation, and the difference with respect to the nominal response matrix is then propagated to the unfolded distribution. The uncertainty in the measurement of the integrated luminosity is estimated to be 1.6% [45–47] and is assigned to the unfolded distribution directly. Statistical uncertainties from the limited size of the simulated samples, denoted by “MC stat”, are included in the experimental uncertainties. The simulated samples for 2017 and 2018 increase the statistical precision of the unfolding compared to the previous measurement with 2016 data only, because of the higher statistical precision in the response matrix, which is obtained using simulated $t\bar{t}$ events. Simulated background processes are used to estimate the amount of background events and are subtracted from data. The corresponding statistical uncertainties in the background samples are much smaller than the uncertainties in the cross sections of these processes, which are 19% for W+jets production, 23% for single top quark production and 100% for other SM backgrounds [94–99]. The statistical uncertainties from the limited size of the MC samples are found to be a factor of more than three smaller compared to the ones from data.

Model uncertainties arise from the choice of parameters in the event simulation. These parameters include the factorisation and renormalisation scales μ_F and μ_R , the top quark mass, the energy scales for the initial state radiation (ISR) and FSR, the matching between matrix element and parton shower (h_{damp}) [66], the colour reconnection, the UE tune and the choice of PDFs. The model parameters are varied within their uncertainties and the corresponding uncertainties in the m_{jet} measurement are estimated as described in the following.

The values of μ_F , μ_R , and the ISR scales are varied by factors from 0.5 to 2. The parameter h_{damp} and the UE tune are varied within their uncertainties [66]. For μ_F and μ_R , there are eight possible combinations to vary the scales. We find that the simultaneous up and down variations of both scales have the largest effects. In order to estimate the uncertainty in the μ_F and μ_R scales, we thus only consider simultaneous shifts of μ_F and μ_R . In order to estimate the uncertainty in the colour reconnection model, three different models [100–102] are considered as variations. The uncertainty due to the choice of PDFs has been found to be negligible in the last measurements of m_{jet} [32, 33] because m_{jet} in fully merged top quark decays is sensitive

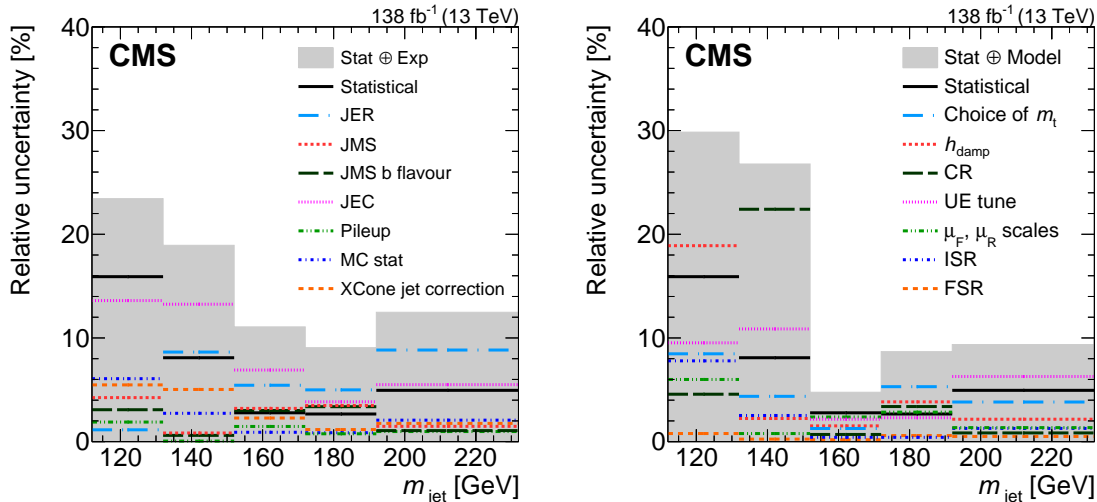


Figure 9: Relative experimental (left) and model (right) uncertainties in the measurement of m_{jet} . Various sources are displayed as coloured lines and compared to the total experimental or model uncertainty, respectively. The uncertainty sources are calculated as the square root of the diagonal entries from the respective covariance matrix, and do not include bin-to-bin correlations.

to the decay of the top quark, but not to the dynamics of its production. Therefore, we do not follow the recommendation for estimating PDF uncertainties using different PDF sets [103], but we estimate the PDF uncertainty by using 100 variations of the NNPDF sets versions 3.0 [62] and 3.1 [63].

For all model variations, the simulated m_{jet} distribution at the detector level is unfolded to the particle level using the same setup as for data. Differences between the true distribution at the particle level and the unfolded simulation with model variations indicate a potential bias in the unfolding setup and are treated as uncertainties. For uncertainties in the ISR scale, the μ_{F} and μ_{R} scales, the h_{damp} parameter, and the UE tune the average bias of the up and down variations is calculated in each bin and taken as an uncertainty. In the case of the colour reconnection model, the impact of a change in the model is calculated by taking the difference in the mean of m_{jet} between the true distribution at the particle level and the unfolded distribution. The model with the largest difference is chosen, and we take the resulting bias as the uncertainty from the colour reconnection model.

The uncertainty due to the choice of m_{t} in the $\text{t}\bar{\text{t}}$ simulation used to unfold the data is calculated using samples with different values of m_{t} . The difference between the unfolded distribution and the true particle-level distribution is parametrised in each bin of the unfolded distribution. We use a linear function with m_{t} as its argument to describe the difference. The parameters of this function are obtained using the $\text{t}\bar{\text{t}}$ samples with $m_{\text{t}} = 169.5, 171.5, 173.5,$ and 175.5 GeV. The uncertainty is then evaluated from the linear function at $m_{\text{t}} = 172.5 \pm 1$ GeV. This procedure has the advantage of being less susceptible to statistical fluctuations in the individual samples, therefore resulting in a more reliable estimate of this uncertainty. The interval of ± 1 GeV has been found to be sufficient, because larger variations do not agree with the data at the detector level.

We use the same method to calculate the uncertainty in the modelling of FSR. The simulated samples with different choices of f_{FSR} are unfolded, and the differences between the true dis-

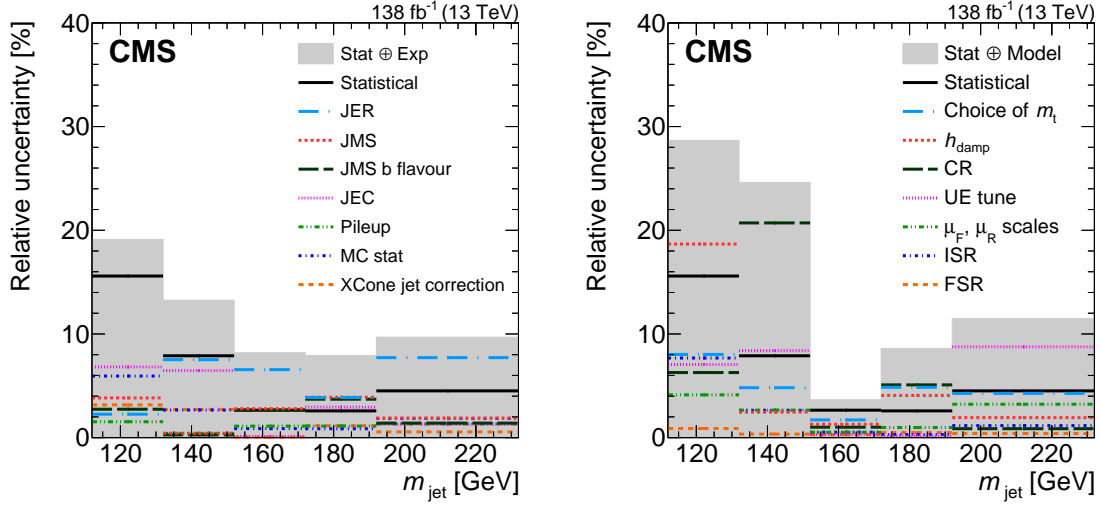


Figure 10: Relative experimental (left) and model (right) uncertainties after normalising the measurement to the total cross section. Various sources are displayed as coloured lines and compared to the total experimental or model uncertainty, respectively. The uncertainty sources are calculated as the square root of the diagonal entries from the respective covariance matrix, and do not include bin-to-bin correlations.

tribution at the particle level and the unfolded distributions are parametrised as a function of f_{FSR} in each bin. The uncertainty is obtained by evaluating the parametrisation at the values obtained in the studies described in Section 8.

Figure 9 summarises the experimental and model uncertainties in the measurement of m_{jet} . The largest experimental uncertainties arise from the JES and JER corrections. In the m_{jet} peak region (the third and fourth bins) the largest sources of model uncertainties are from the UE tune, the h_{damp} parameter, and the choice of m_t . In the first two bins, the limited statistical precision of the samples with model variations, in combination with a smaller number of observed events than in the peak region, leads to statistical fluctuations in the estimation of model uncertainties. This results in large uncertainties from h_{damp} and the colour reconnection models in the first and second bins of the measurement, respectively. Because the sensitivity to m_t of the m_{jet} measurement comes from the peak region, these uncertainties have a minor effect on the determination of m_t .

When normalising the unfolded distribution, systematic uncertainties cancel fully or partially. For example, the uncertainty in the integrated luminosity cancels completely as it affects all bins by an equal amount. The uncertainty component in the JEC that changes only the three-vector predominantly changes the X Cone jet p_T , and thus affects the selection efficiency of the measurement. This uncertainty cancels to a large part when normalising the measurement and becomes negligible. The uncertainties in the normalised measurement are summarized in Fig. 10. In the peak region, the dominant experimental uncertainties originate from JER and JMS corrections. The dominant model uncertainties are the same as for the absolute cross section measurement.

Theory uncertainties are those uncertainties that apply to predictions at the particle level. The scales for FSR, ISR, μ_F and μ_R , as well as h_{damp} and the UE tune are varied as before. All three models of colour reconnection are used to calculate the corresponding uncertainty. For each source, the uncertainty in each bin is estimated by the largest difference to the nominal prediction at the particle level.

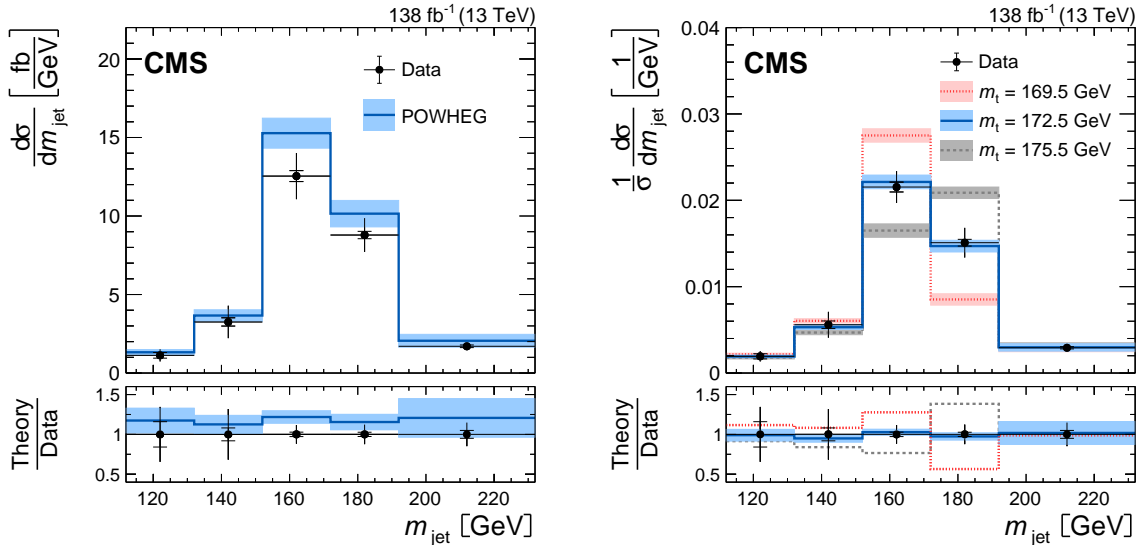


Figure 11: Differential $t\bar{t}$ production cross section as a function of m_{jet} compared to predictions obtained with POWHEG: absolute (left) and normalised (right). For the normalised measurement, the data are compared to predictions with different m_t . The vertical bars represent the total uncertainties, and the statistical uncertainties are shown by short horizontal bars. The long horizontal bars reflect the bin widths. Theoretical uncertainties in the prediction are indicated by the bands. The lower panels show the ratio of the theoretical prediction to data.

11 Results and determination of the top quark mass

The three different years, as well as the electron and muon channels, are combined before the unfolding, but are also processed individually to validate their consistency. Figure 11 (left) shows the differential $t\bar{t}$ cross section in the fiducial region as a function of m_{jet} , measured in data and compared to simulation. The $t\bar{t}$ production cross section in the fiducial region is measured to be 582 ± 8 (stat) ± 46 (exp) ± 21 (model) fb. This can be compared to the prediction from the POWHEG simulation, 690 ± 59 fb. The smaller value of the measured cross section compared to the prediction from POWHEG at NLO has been observed in other analyses for top quark $p_T > 400$ GeV [87–89], where NNLO calculations describe the shape of the top quark p_T distribution better.

We determine the value of m_t from the normalised differential $t\bar{t}$ production cross section as a function of m_{jet} . This enables a measurement using the shape of the m_{jet} distribution without sensitivity to uncertainties in the normalisation. Figure 11 (right) shows the normalised measurement compared to predictions from POWHEG with different values of m_t . In order to extract m_t , a fit is performed based on $\chi_m^2 = d_m^T V_m^{-1} d_m$, where d_m is the vector of differences between the measured normalised differential cross section and the POWHEG simulation with different values of m_t . Four of the five bins in m_{jet} are used in the calculation of d_m , because of the normalisation of the measurement. The covariance matrix V_m contains all statistical, experimental, model, and theory uncertainties. We use the Linear Template Fit [104] package to parametrise the cross section as a function of m_t and obtain the best fit value with the corresponding uncertainties analytically.

The bin-to-bin correlations in the measurement calculated from V_m , including statistical, experimental, and model contributions, are displayed in Fig. 12. Negative correlations between neighbouring bins originate from migrations at the detector level, which have been corrected

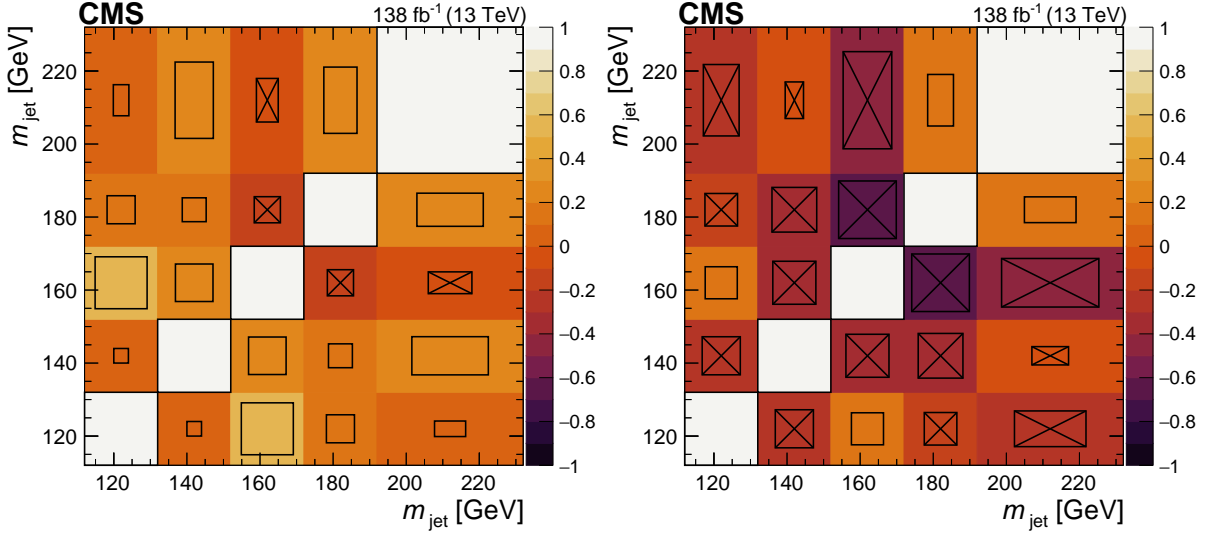


Figure 12: Correlations between the bins in the unfolding before (left) and after (right) normalising the distribution to the total cross section. Boxes with crosses indicate negative values of the correlation coefficient.

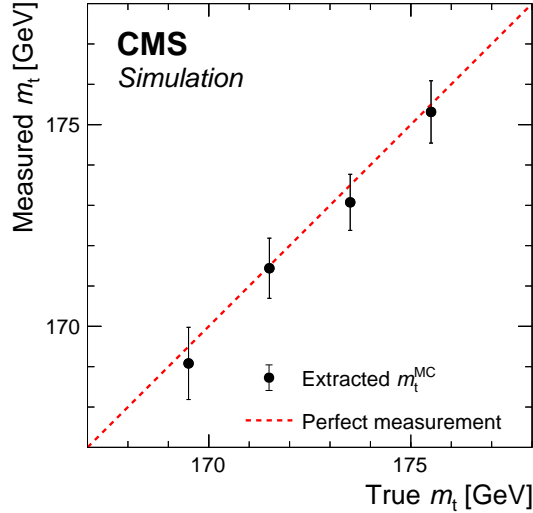


Figure 13: Extracted top quark mass from simulation compared to the true value. The vertical error bars show the total uncertainty in the extraction of m_t .

for by the unfolding and result in anticorrelated statistical uncertainties. The systematic variations that shift the peak of the m_{jet} distribution, for example the JMS, also contribute to the negative correlations.

In order to validate that the determination of m_t is unbiased, we perform the m_t measurement using simulated samples with various values of m_t . The obtained value of m_t is compared to the true value in Fig. 13. In this comparison, all extracted values agree with the respective true values of m_t , demonstrating the validity of the mass extraction.

Performing the extraction on collision data and considering all sources of uncertainties, we

Table 1: Total and individual uncertainties in the extraction of m_t from the normalised differential cross section. The uncertainties are grouped into experimental, model, theory, and statistical uncertainties. Uncertainties from the choice of the PDF, b tagging, the luminosity measurement, and the lepton triggers, identification and reconstruction are smaller than 0.01 GeV and are not listed.

Source	Uncertainty [GeV]
Jet energy resolution	0.40
Jet mass scale	0.27
Jet mass scale b flavour	0.27
Jet energy scale	0.09
Pileup	0.08
MC stat	0.07
Additional X Cone corrections	0.03
Backgrounds	0.01
Experimental total	0.57
Choice of m_t	0.37
h_{damp}	0.19
Colour reconnection	0.19
Underlying event tune	0.12
μ_F, μ_R scales	0.07
ISR	0.06
FSR	0.03
Model total	0.48
FSR	0.14
Underlying event tune	0.13
Colour reconnection	0.10
μ_F, μ_R scales	0.06
h_{damp}	0.06
ISR	0.06
Theory total	0.24
Statistical	0.22
Total	0.81

extract m_t using the POWHEG simulation,

$$\begin{aligned}
 m_t &= 172.76 \pm 0.22 \text{ (stat)} \pm 0.57 \text{ (exp)} \pm 0.48 \text{ (model)} \pm 0.24 \text{ (theo)} \text{ GeV} \\
 &= 172.76 \pm 0.81 \text{ GeV.}
 \end{aligned}$$

With respect to the previous CMS measurement at 13 TeV [33], this corresponds to an improvement by more than a factor of three in terms of precision. This measurement from boosted top quark production has an uncertainty comparable with the most precise m_t extractions from fully resolved final states [9–15].

The individual sources of uncertainty and their impact on the mass extraction are detailed in Table 1. The dominant experimental uncertainties are connected to the calibration of the JER,

the JMS calibration, and the JMS b flavour uncertainty, also visible in Fig. 10. The dominant modelling uncertainties arise from the choice of the m_t and h_{damp} parameters in the $t\bar{t}$ simulation. Compared to the previous measurement, the dedicated measurement of the JMS leads to an uncertainty reduced by a factor of 5 in the jet calibration. By constraining the simulation of FSR with data, this previously dominant model uncertainty becomes small. The use of about four times the data, corresponding to an integrated luminosity of 138 fb^{-1} , leads to a reduction in the statistical uncertainty by a factor of 2.

The improvements described in this article result in a considerable gain in precision, allowing for a determination of m_t from $t\bar{t}$ production at high p_T with an uncertainty comparable to the one achieved in measurements close to the $t\bar{t}$ production threshold with fully resolved final state objects. The measurement also provides important information on the modelling of the jet mass in decays of boosted top quarks, which is the most important substructure variable for the identification of large-radius jets [105].

12 Conclusions

A measurement of the differential top quark pair ($t\bar{t}$) production cross section as a function of the jet mass m_{jet} in hadronic decays of boosted top quarks has been presented. The normalised distribution in m_{jet} is sensitive to the top quark mass m_t , which is measured to be $172.76 \pm 0.81 \text{ GeV}$. This value is compatible with earlier precision measurements in fully resolved final states [11, 14, 15]. With respect to an earlier CMS analysis [33], the precision is improved by a factor of more than three. This has been achieved by a dedicated calibration of the jet mass scale, a study of the effects of final state radiation inside large-radius jets, and about 4 times more data. With these improvements, the uncertainty in the extraction of m_t at high top quark boosts becomes comparable to direct measurements close to the $t\bar{t}$ production threshold. The sources of the leading systematic uncertainties are very different, highlighting the complementarity of this measurement. In addition, the study of boosted top quarks offers the possibility to directly compare the distribution in m_{jet} to analytic calculations [30]. When these calculations become available, the unfolded m_{jet} distribution can be used to measure the top quark pole mass directly. The precisely measured differential cross section as a function of m_{jet} represents an important step towards understanding and resolving the ambiguities between the top quark mass extracted from a direct reconstruction of m_t , and the top quark pole mass.

References

- [1] CDF Collaboration, “Observation of top quark production in $\bar{p}p$ collisions”, *Phys. Rev. Lett.* **74** (1995) 2626, doi:10.1103/PhysRevLett.74.2626, arXiv:hep-ex/9503002.
- [2] D0 Collaboration, “Observation of the top quark”, *Phys. Rev. Lett.* **74** (1995) 2632, doi:10.1103/PhysRevLett.74.2632, arXiv:hep-ex/9503003.
- [3] ALEPH, CDF, D0, DELPHI, L3, OPAL, and SLD Collaborations, the LEP Electroweak Working Group, the Tevatron Electroweak Working Group, and the SLD Electroweak and Heavy Flavour Groups, “Precision electroweak measurements and constraints on the standard model”, 2010. arXiv:1012.2367.

- [4] J. Haller et al., “Update of the global electroweak fit and constraints on two-Higgs-doublet models”, *Eur. Phys. J. C* **78** (2018) 675, doi:10.1140/epjc/s10052-018-6131-3, arXiv:1803.01853.
- [5] Particle Data Group, P. A. Zyla et al., “Review of particle physics”, *Prog. Theor. Exp. Phys.* **2020** (2020) 083C01, doi:10.1093/ptep/ptaa104.
- [6] G. Degrandi et al., “Higgs mass and vacuum stability in the standard model at NNLO”, *JHEP* **08** (2012) 098, doi:10.1007/JHEP08(2012)098, arXiv:1205.6497.
- [7] F. Bezrukov, M. Y. Kalmykov, B. A. Kniehl, and M. Shaposhnikov, “Higgs boson mass and new physics”, *JHEP* **10** (2012) 140, doi:10.1007/JHEP10(2012)140, arXiv:1205.2893.
- [8] A. V. Bednyakov, B. A. Kniehl, A. F. Pikelner, and O. L. Veretin, “Stability of the electroweak vacuum: Gauge independence and advanced precision”, *Phys. Rev. Lett.* **115** (2015) 201802, doi:10.1103/PhysRevLett.115.201802, arXiv:1507.08833.
- [9] ATLAS Collaboration, “Measurement of the top quark mass in the $t\bar{t} \rightarrow$ dilepton channel from $\sqrt{s} = 8$ TeV ATLAS data”, *Phys. Lett. B* **761** (2016) 350, doi:10.1016/j.physletb.2016.08.042, arXiv:1606.02179.
- [10] ATLAS Collaboration, “Top-quark mass measurement in the all-hadronic $t\bar{t}$ decay channel at $\sqrt{s} = 8$ TeV with the ATLAS detector”, *JHEP* **09** (2017) 118, doi:10.1007/JHEP09(2017)118, arXiv:1702.07546.
- [11] ATLAS Collaboration, “Measurement of the top quark mass in the $t\bar{t} \rightarrow$ lepton+jets channel from $\sqrt{s} = 8$ TeV ATLAS data and combination with previous results”, *Eur. Phys. J. C* **79** (2019) 290, doi:10.1140/epjc/s10052-019-6757-9, arXiv:1810.01772.
- [12] CMS Collaboration, “Measurement of the top quark mass using proton-proton data at $\sqrt{s} = 7$ and 8 TeV”, *Phys. Rev. D* **93** (2016) 072004, doi:10.1103/PhysRevD.93.072004, arXiv:1509.04044.
- [13] CMS Collaboration, “Measurement of the top quark mass in the dileptonic $t\bar{t}$ decay channel using the mass observables $M_{b\ell}$, M_{T2} , and $M_{b\ell\nu}$ in pp collisions at $\sqrt{s} = 8$ TeV”, *Phys. Rev. D* **96** (2017) 032002, doi:10.1103/PhysRevD.96.032002, arXiv:1704.06142.
- [14] CMS Collaboration, “Measurement of the top quark mass with lepton+jets final states using pp collisions at $\sqrt{s} = 13$ TeV”, *Eur. Phys. J. C* **78** (2018) 891, doi:10.1140/epjc/s10052-018-6332-9, arXiv:1805.01428.
- [15] CMS Collaboration, “Measurement of the top quark mass in the all-jets final state at $\sqrt{s} = 13$ TeV and combination with the lepton+jets channel”, *Eur. Phys. J. C* **79** (2019) 313, doi:10.1140/epjc/s10052-019-6788-2, arXiv:1812.10534.
- [16] A. H. Hoang et al., “The MSR mass and the $\mathcal{O}(\Lambda_{\text{qcd}})$ renormalon sum rule”, *JHEP* **04** (2018) 003, doi:10.1007/JHEP04(2018)003, arXiv:1704.01580.
- [17] A. H. Hoang, “What is the top quark mass?”, *Ann. Rev. Nucl. Part. Sci.* **70** (2020) 225, doi:10.1146/annurev-nucl-101918-023530, arXiv:2004.12915.

- [18] D0 Collaboration, “Determination of the pole and \overline{MS} masses of the top quark from the $t\bar{t}$ cross section”, *Phys. Lett. B* **703** (2011) 422, doi:10.1016/j.physletb.2011.08.015, arXiv:1104.2887.
- [19] D0 Collaboration, “Measurement of the inclusive $t\bar{t}$ production cross section in $p\bar{p}$ collisions at $\sqrt{s} = 1.96$ TeV and determination of the top quark pole mass”, *Phys. Rev. D* **94** (2016) 092004, doi:10.1103/PhysRevD.94.092004, arXiv:1605.06168.
- [20] ATLAS Collaboration, “Measurement of the $t\bar{t}$ production cross-section using $e\mu$ events with b-tagged jets in pp collisions at $\sqrt{s} = 7$ and 8 TeV with the ATLAS detector”, *Eur. Phys. J. C* **74** (2014) 3109, doi:10.1140/epjc/s10052-014-3109-7, arXiv:1406.5375. [Addendum: doi:10.1140/epjc/s10052-016-4501-2].
- [21] ATLAS Collaboration, “Measurement of lepton differential distributions and the top quark mass in $t\bar{t}$ production in pp collisions at $\sqrt{s} = 8$ TeV with the ATLAS detector”, *Eur. Phys. J. C* **77** (2017) 804, doi:10.1140/epjc/s10052-017-5349-9, arXiv:1709.09407.
- [22] ATLAS Collaboration, “Measurement of the $t\bar{t}$ production cross-section and lepton differential distributions in $e\mu$ dilepton events from pp collisions at $\sqrt{s} = 13$ TeV with the ATLAS detector”, *Eur. Phys. J. C* **80** (2020) 528, doi:10.1140/epjc/s10052-020-7907-9, arXiv:1910.08819.
- [23] CMS Collaboration, “Determination of the top-quark pole mass and strong coupling constant from the $t\bar{t}$ production cross section in pp collisions at $\sqrt{s} = 7$ TeV”, *Phys. Lett. B* **728** (2014) 496, doi:10.1016/j.physletb.2013.12.009, arXiv:1307.1907. [Erratum: doi:10.1016/j.physletb.2014.08.040].
- [24] CMS Collaboration, “Measurement of the $t\bar{t}$ production cross section in the $e\mu$ channel in proton-proton collisions at $\sqrt{s} = 7$ and 8 TeV”, *JHEP* **08** (2016) 029, doi:10.1007/JHEP08(2016)029, arXiv:1603.02303.
- [25] CMS Collaboration, “Measurement of the $t\bar{t}$ production cross section, the top quark mass, and the strong coupling constant using dilepton events in pp collisions at $\sqrt{s} = 13$ TeV”, *Eur. Phys. J. C* **79** (2019) 368, doi:10.1140/epjc/s10052-019-6863-8, arXiv:1812.10505.
- [26] CMS Collaboration, “Measurement of $t\bar{t}$ normalised multi-differential cross sections in pp collisions at $\sqrt{s} = 13$ TeV, and simultaneous determination of the strong coupling strength, top quark pole mass, and parton distribution functions”, *Eur. Phys. J. C* **80** (2020) 658, doi:10.1140/epjc/s10052-020-7917-7, arXiv:1904.05237.
- [27] A. J. Larkoski, I. Moult, and B. Nachman, “Jet substructure at the Large Hadron Collider: A review of recent advances in theory and machine learning”, *Phys. Rep.* **841** (2020) 1, doi:10.1016/j.physrep.2019.11.001, arXiv:1709.04464.
- [28] R. Kogler et al., “Jet substructure at the large hadron collider”, *Rev. Mod. Phys.* **91** (2019) 045003, doi:10.1103/RevModPhys.91.045003, arXiv:1803.06991.
- [29] R. Kogler, “Advances in jet substructure at the LHC: Algorithms, measurements and searches for new physical phenomena”, volume 284 of *Springer Tracts Mod. Phys.* Springer, 2021. doi:10.1007/978-3-030-72858-8, ISBN 978-3-030-72857-1, 978-3-030-72858-8.

- [30] A. H. Hoang, S. Mantry, A. Pathak, and I. W. Stewart, “Extracting a short distance top mass with light grooming”, *Phys. Rev. D* **100** (2019) 074021, doi:10.1103/PhysRevD.100.074021, arXiv:1708.02586.
- [31] CMS Collaboration, “Measurement of the top quark pole mass using $t\bar{t}$ -jet events in the dilepton final state in proton-proton collisions at $\sqrt{s} = 13$ TeV”, 2022. arXiv:2207.02270. Submitted to *JHEP*.
- [32] CMS Collaboration, “Measurement of the jet mass in highly boosted $t\bar{t}$ events from pp collisions at $\sqrt{s} = 8$ TeV”, *Eur. Phys. J. C* **77** (2017) 467, doi:10.1140/epjc/s10052-017-5030-3, arXiv:1703.06330.
- [33] CMS Collaboration, “Measurement of the jet mass distribution and top quark mass in hadronic decays of boosted top quarks in pp collisions at $\sqrt{s} = 13$ TeV”, *Phys. Rev. Lett.* **124** (2020) 202001, doi:10.1103/PhysRevLett.124.202001, arXiv:1911.03800.
- [34] CMS Collaboration, “Determination of jet energy calibration and transverse momentum resolution in CMS”, *JINST* **6** (2011) P11002, doi:10.1088/1748-0221/6/11/P11002, arXiv:1107.4277.
- [35] CMS Collaboration, “Jet energy scale and resolution in the CMS experiment in pp collisions at 8 TeV”, *JINST* **12** (2017) P02014, doi:10.1088/1748-0221/12/02/P02014, arXiv:1607.03663.
- [36] J. Thaler and K. Van Tilburg, “Identifying boosted objects with N -subjettiness”, *JHEP* **03** (2011) 015, doi:10.1007/JHEP03(2011)015, arXiv:1011.2268.
- [37] J. Thaler and K. Van Tilburg, “Maximizing boosted top identification by minimizing N -subjettiness”, *JHEP* **02** (2012) 093, doi:10.1007/JHEP02(2012)093, arXiv:1108.2701.
- [38] P. Skands, S. Carrazza, and J. Rojo, “Tuning PYTHIA 8.1: The Monash 2013 Tune”, *Eur. Phys. J. C* **74** (2014) 3024, doi:10.1140/epjc/s10052-014-3024-y, arXiv:1404.5630.
- [39] CMS Collaboration, “Measurement of jet substructure observables in $t\bar{t}$ events from proton-proton collisions at $\sqrt{s} = 13$ TeV”, *Phys. Rev. D* **98** (2018) 092014, doi:10.1103/PhysRevD.98.092014, arXiv:1808.07340.
- [40] HEPData record for this analysis, 2022. doi:10.17182/hepdata.130712.
- [41] CMS Collaboration, “The CMS experiment at the CERN LHC”, *JINST* **3** (2008) S08004, doi:10.1088/1748-0221/3/08/S08004.
- [42] Tracker Group of the CMS Collaboration, “The CMS Phase-1 pixel detector upgrade”, *JINST* **16** (2021) P02027, doi:10.1088/1748-0221/16/02/P02027, arXiv:2012.14304.
- [43] CMS Collaboration, “Performance of the CMS Level-1 trigger in proton-proton collisions at $\sqrt{s} = 13$ TeV”, *JINST* **15** (2020) P10017, doi:10.1088/1748-0221/15/10/P10017, arXiv:2006.10165.
- [44] CMS Collaboration, “The CMS trigger system”, *JINST* **12** (2017) P01020, doi:10.1088/1748-0221/12/01/P01020, arXiv:1609.02366.

-
- [45] CMS Collaboration, “Precision luminosity measurement in proton-proton collisions at $\sqrt{s} = 13$ TeV in 2015 and 2016 at CMS”, *Eur. Phys. J. C* **81** (2021) 800, doi:10.1140/epjc/s10052-021-09538-2, arXiv:2104.01927.
- [46] CMS Collaboration, “CMS luminosity measurement for the 2017 data-taking period at $\sqrt{s} = 13$ TeV”, CMS Physics Analysis Summary CMS-PAS-LUM-17-004, 2018.
- [47] CMS Collaboration, “CMS luminosity measurement for the 2018 data-taking period at $\sqrt{s} = 13$ TeV”, CMS Physics Analysis Summary CMS-PAS-LUM-18-002, 2019.
- [48] P. Nason, “A new method for combining NLO QCD with shower Monte Carlo algorithms”, *JHEP* **11** (2004) 040, doi:10.1088/1126-6708/2004/11/040, arXiv:hep-ph/0409146.
- [49] S. Frixione, P. Nason, and C. Oleari, “Matching NLO QCD computations with parton shower simulations: the POWHEG method”, *JHEP* **11** (2007) 070, doi:10.1088/1126-6708/2007/11/070, arXiv:0709.2092.
- [50] S. Alioli, P. Nason, C. Oleari, and E. Re, “A general framework for implementing NLO calculations in shower Monte Carlo programs: the POWHEG BOX”, *JHEP* **06** (2010) 043, doi:10.1007/JHEP06(2010)043, arXiv:1002.2581.
- [51] S. Frixione, P. Nason, and G. Ridolfi, “A positive-weight next-to-leading-order Monte Carlo for heavy flavour hadroproduction”, *JHEP* **09** (2007) 126, doi:10.1088/1126-6708/2007/09/126, arXiv:0707.3088.
- [52] S. Alioli, P. Nason, C. Oleari, and E. Re, “NLO single-top production matched with shower in POWHEG: s - and t -channel contributions”, *JHEP* **09** (2009) 111, doi:10.1088/1126-6708/2009/09/111, arXiv:0907.4076. [Erratum: doi:10.1007/JHEP02(2010)011].
- [53] E. Re, “Single-top W -channel production matched with parton showers using the POWHEG method”, *Eur. Phys. J. C* **71** (2011) 1547, doi:10.1140/epjc/s10052-011-1547-z, arXiv:1009.2450.
- [54] M. Czakon and A. Mitov, “Top++: A program for the calculation of the top-pair cross-section at hadron colliders”, *Comput. Phys. Commun.* **185** (2014) 2930, doi:10.1016/j.cpc.2014.06.021, arXiv:1112.5675.
- [55] J. Alwall et al., “The automated computation of tree-level and next-to-leading order differential cross sections, and their matching to parton shower simulations”, *JHEP* **07** (2014) 079, doi:10.1007/JHEP07(2014)079, arXiv:1405.0301.
- [56] S. Frixione and B. R. Webber, “Matching NLO QCD computations and parton shower simulations”, *JHEP* **06** (2002) 029, doi:10.1088/1126-6708/2002/06/029, arXiv:hep-ph/0204244.
- [57] N. Kidonakis, “Two-loop soft anomalous dimensions for single top quark associated production with a W^- or H^- ”, *Phys. Rev. D* **82** (2010) 054018, doi:10.1103/PhysRevD.82.054018, arXiv:1005.4451.
- [58] N. Kidonakis, “Top quark production”, in *Helmholtz International Summer School on Physics of Heavy Quarks and Hadrons*. 2013. arXiv:1311.0283. doi:10.3204/DESY-PROC-2013-03/Kidonakis.

- [59] M. Aliev et al., “HATHOR — HAdronic Top and Heavy quarks crOss section calculatoR”, *Comput. Phys. Commun.* **182** (2011) 1034, doi:10.1016/j.cpc.2010.12.040, arXiv:1007.1327.
- [60] Y. Li and F. Petriello, “Combining QCD and electroweak corrections to dilepton production in FEWZ”, *Phys. Rev. D* **86** (2012) 094034, doi:10.1103/PhysRevD.86.094034, arXiv:1208.5967.
- [61] T. Sjöstrand et al., “An introduction to PYTHIA 8.2”, *Comput. Phys. Commun.* **191** (2015) 159, doi:10.1016/j.cpc.2015.01.024, arXiv:1410.3012.
- [62] NNPDF Collaboration, “Parton distributions for the LHC Run II”, *JHEP* **04** (2015) 040, doi:10.1007/JHEP04(2015)040, arXiv:1410.8849.
- [63] NNPDF Collaboration, “Parton distributions from high-precision collider data”, *Eur. Phys. J. C* **77** (2017) 663, doi:10.1140/epjc/s10052-017-5199-5, arXiv:1706.00428.
- [64] R. Frederix and S. Frixione, “Merging meets matching in MC@NLO”, *JHEP* **12** (2012) 061, doi:10.1007/JHEP12(2012)061, arXiv:1209.6215.
- [65] J. Alwall et al., “Comparative study of various algorithms for the merging of parton showers and matrix elements in hadronic collisions”, *Eur. Phys. J. C* **53** (2008) 473, doi:10.1140/epjc/s10052-007-0490-5, arXiv:0706.2569.
- [66] CMS Collaboration, “Extraction and validation of a new set of CMS PYTHIA8 tunes from underlying-event measurements”, *Eur. Phys. J. C* **80** (2020) 4, doi:10.1140/epjc/s10052-019-7499-4, arXiv:1903.12179.
- [67] CMS Collaboration, “Event generator tunes obtained from underlying event and multiparton scattering measurements”, *Eur. Phys. J. C* **76** (2016) 155, doi:10.1140/epjc/s10052-016-3988-x, arXiv:1512.00815.
- [68] GEANT4 Collaboration, “GEANT4 — A simulation toolkit”, *Nucl. Instrum. Meth. A* **506** (2003) 250, doi:10.1016/S0168-9002(03)01368-8.
- [69] J. Allison et al., “GEANT4 developments and applications”, *IEEE Trans. Nucl. Sci.* **53** (2006) 270, doi:10.1109/TNS.2006.869826.
- [70] CMS Collaboration, “Measurement of the inelastic proton-proton cross section at $\sqrt{s} = 13$ TeV”, *JHEP* **07** (2018) 161, doi:10.1007/JHEP07(2018)161, arXiv:1802.02613.
- [71] CMS Collaboration, “Particle-flow reconstruction and global event description with the CMS detector”, *JINST* **12** (2017) P10003, doi:10.1088/1748-0221/12/10/P10003, arXiv:1706.04965.
- [72] M. Cacciari, G. P. Salam, and G. Soyez, “The anti- k_T jet clustering algorithm”, *JHEP* **04** (2008) 063, doi:10.1088/1126-6708/2008/04/063, arXiv:0802.1189.
- [73] M. Cacciari, G. P. Salam, and G. Soyez, “Fastjet user manual”, *Eur. Phys. J. C* **72** (2012) 1896, doi:10.1140/epjc/s10052-012-1896-2, arXiv:1111.6097.
- [74] CMS Collaboration, “Technical proposal for the Phase-II upgrade of the Compact Muon Solenoid”, CMS Technical Proposal CERN-LHCC-2015-010, CMS-TDR-15-02, 2015.

-
- [75] CMS Collaboration, “Performance of the CMS muon detector and muon reconstruction with proton-proton collisions at $\sqrt{s} = 13$ TeV”, *JINST* **13** (2018) P06015, doi:10.1088/1748-0221/13/06/P06015, arXiv:1804.04528.
- [76] CMS Collaboration, “Electron and photon reconstruction and identification with the CMS experiment at the CERN LHC”, *JINST* **16** (2021) P05014, doi:10.1088/1748-0221/16/05/P05014, arXiv:2012.06888.
- [77] I. W. Stewart et al., “XCone: N -jettiness as an exclusive cone jet algorithm”, *JHEP* **11** (2015) 072, doi:10.1007/JHEP11(2015)072, arXiv:1508.01516.
- [78] J. Thaler and T. F. Wilkason, “Resolving boosted jets with XCone”, *JHEP* **12** (2015) 051, doi:10.1007/JHEP12(2015)051, arXiv:1508.01518.
- [79] D. Krohn, J. Thaler, and L.-T. Wang, “Jet trimming”, *JHEP* **02** (2010) 084, doi:10.1007/JHEP02(2010)084, arXiv:0912.1342.
- [80] Y. L. Dokshitzer, G. D. Leder, S. Moretti, and B. R. Webber, “Better jet clustering algorithms”, *JHEP* **08** (1997) 001, doi:10.1088/1126-6708/1997/08/001, arXiv:hep-ph/9707323.
- [81] M. Wobisch and T. Wengler, “Hadronization corrections to jet cross sections in deep-inelastic scattering”, in *Workshop on Monte Carlo generators for HERA physics*. DESY, Hamburg, Germany, 1998. arXiv:hep-ph/9907280.
- [82] CMS Collaboration, “Search for resonant $t\bar{t}$ production in proton-proton collisions at $\sqrt{s} = 13$ TeV”, *JHEP* **04** (2019) 031, doi:10.1007/JHEP04(2019)031, arXiv:1810.05905.
- [83] CMS Collaboration, “Search for a heavy resonance decaying to a top quark and a vector-like top quark in the lepton+jets final state in pp collisions at $\sqrt{s} = 13$ TeV”, *Eur. Phys. J. C* **79** (2019) 208, doi:10.1140/epjc/s10052-019-6688-5, arXiv:1812.06489.
- [84] CMS Collaboration, “Performance of b tagging algorithms in proton-proton collisions at 13 TeV with Phase 1 CMS detector”, CMS Detector Performance Note CMS-DP-2018-033, 2018.
- [85] E. Bols et al., “Jet flavour classification using DeepJet”, *JINST* **15** (2020) P12012, doi:10.1088/1748-0221/15/12/P12012, arXiv:2008.10519.
- [86] CMS Collaboration, “Performance of missing transverse momentum reconstruction in proton-proton collisions at $\sqrt{s} = 13$ TeV using the CMS detector”, *JINST* **14** (2019) P07004, doi:10.1088/1748-0221/14/07/P07004, arXiv:1903.06078.
- [87] CMS Collaboration, “Measurement of differential $t\bar{t}$ production cross sections in the full kinematic range using lepton+jets events from proton-proton collisions at $\sqrt{s} = 13$ TeV”, *Phys. Rev. D* **104** (2021) 092013, doi:10.1103/PhysRevD.104.092013, arXiv:2108.02803.
- [88] ATLAS Collaboration, “Measurements of differential cross-sections in top-quark pair events with a high transverse momentum top quark and limits on beyond the standard model contributions to top-quark pair production with the ATLAS detector at $\sqrt{s} = 13$ TeV”, *JHEP* **06** (2022) 063, doi:10.1007/JHEP06(2022)063, arXiv:2202.12134.

- [89] ATLAS Collaboration, “Differential $t\bar{t}$ cross-section measurements using boosted top quarks in the all-hadronic final state with 139 fb^{-1} of ATLAS data”, 2022. arXiv:2205.02817.
- [90] F. Herren and M. Steinhauser, “Version 3 of RunDec and CRunDec”, *Comput. Phys. Commun.* **224** (2018) 333, doi:10.1016/j.cpc.2017.11.014, arXiv:1703.03751.
- [91] S. Schmitt, “TUnfold: An algorithm for correcting migration effects in high energy physics”, *JINST* **7** (2012) T10003, doi:10.1088/1748-0221/7/10/T10003, arXiv:1205.6201.
- [92] S. Schmitt, “Data unfolding methods in high energy physics”, in *12th Conference on Quark Confinement and the Hadron Spectrum. Confinement XII*, Thessaloniki, Greece, 2016. arXiv:1611.01927.
- [93] CMS Collaboration, “Identification of heavy-flavour jets with the CMS detector in pp collisions at 13 TeV”, *JINST* **13** (2018) P05011, doi:10.1088/1748-0221/13/05/P05011, arXiv:1712.07158.
- [94] CMS Collaboration, “Measurement of the $t\bar{t}$ production cross section using events in the $e\mu$ final state in pp collisions at $\sqrt{s} = 13 \text{ TeV}$ ”, *Eur. Phys. J. C* **77** (2017) 172, doi:10.1140/epjc/s10052-017-4718-8, arXiv:1611.04040.
- [95] CMS Collaboration, “Measurement of inclusive W and Z boson production cross sections in pp collisions at $\sqrt{s} = 8 \text{ TeV}$ ”, *Phys. Rev. Lett.* **112** (2014) 191802, doi:10.1103/PhysRevLett.112.191802, arXiv:1402.0923.
- [96] CMS Collaboration, “Cross section measurement of t -channel single top quark production in pp collisions at $\sqrt{s} = 13 \text{ TeV}$ ”, *Phys. Lett. B* **772** (2017) 752, doi:10.1016/j.physletb.2017.07.047, arXiv:1610.00678.
- [97] N. Kidonakis, “NNLL threshold resummation for top-pair and single-top production”, *Phys. Part. Nucl.* **45** (2014) 714, doi:10.1134/S1063779614040091, arXiv:1210.7813.
- [98] T. Gehrmann et al., “ W^+W^- production at hadron colliders in next-to-next-to-leading order QCD”, *Phys. Rev. Lett.* **113** (2014) 212001, doi:10.1103/PhysRevLett.113.212001, arXiv:1408.5243.
- [99] CMS Collaboration, “Measurement of the WZ production cross section in pp collisions at $\sqrt{s} = 13 \text{ TeV}$ ”, *Phys. Lett. B* **766** (2017) 268, doi:10.1016/j.physletb.2017.01.011, arXiv:1607.06943.
- [100] T. Sjöstrand and M. van Zijl, “A multiple interaction model for the event structure in hadron collisions”, *Phys. Rev. D* **36** (1987) 2019, doi:10.1103/PhysRevD.36.2019.
- [101] S. Argyropoulos and T. Sjöstrand, “Effects of color reconnection on $t\bar{t}$ final states at the LHC”, *JHEP* **11** (2014) 043, doi:10.1007/JHEP11(2014)043, arXiv:1407.6653.
- [102] J. R. Christiansen and P. Z. Skands, “String formation beyond leading colour”, *JHEP* **08** (2015) 003, doi:10.1007/JHEP08(2015)003, arXiv:1505.01681.
- [103] J. Butterworth et al., “PDF4LHC recommendations for LHC Run II”, *J. Phys. G* **43** (2016) 023001, doi:10.1088/0954-3899/43/2/023001, arXiv:1510.03865.

- [104] D. Britzger, “The linear template fit”, *Eur. Phys. J. C* **82** (2022) 731,
doi:10.1140/epjc/s10052-022-10581-w, arXiv:2112.01548.
- [105] CMS Collaboration, “Identification of heavy, energetic, hadronically decaying particles using machine-learning techniques”, *JINST* **15** (2020) P06005,
doi:10.1088/1748-0221/15/06/P06005, arXiv:2004.08262.